

Imaging the itinerant-to-localized transmutation of electrons across the metal-to-insulator transition in V_2O_3

Maximilian Thees,¹ Min-Han Lee,² Rosa Luca Bouwmeester,³
Pedro H. Rezende-Gonçalves,^{1,4} Emma David,¹ Alexandre Zimmers,⁵ Franck Fortuna,¹
Emmanouil Frantzeskakis,¹ Nicolas M. Vargas,² Yoav Kalcheim,^{2,6} Patrick Le Fèvre,⁷
Koji Horiba,⁸ Hiroshi Kumigashira,^{9,8} Silke Biermann,^{10,11,12} Juan Trastoy,¹³
Marcelo J. Rozenberg,¹⁴ Ivan K. Schuller,² and Andrés F. Santander-Syro^{1,*}

¹*Université Paris-Saclay, CNRS, Institut des
Sciences Moléculaires d'Orsay, 91405, Orsay, France*

²*Department of Physics and Center for Advanced Nanoscience,
University of California, San Diego, La Jolla, California 92093, USA*

³*Faculty of Science and Technology and MESA+ Institute for Nanotechnology,
University of Twente, 7500 AE Enschede, The Netherlands*

⁴*Departamento de Física, Universidade Federal de Minas Gerais,
Av. Pres. Antonio Carlos, 6627, Belo Horizonte, Brazil*

⁵*LPEM, ESPCI Paris, PSL Research University,
CNRS, Sorbonne Université, 75005 Paris, France*

⁶*Department of Materials Science and Engineering,
Technion - Israel Institute of Technology, Haifa 3200003, Israel*

⁷*Synchrotron SOLEIL, L'Orme des Merisiers,
Saint-Aubin-BP48, 91192 Gif-sur-Yvette, France*

⁸*Photon Factory, Institute of Materials Structure Science,
High Energy Accelerator Research Organization (KEK),
1-1 Oho, Tsukuba 305-0801, Japan*

⁹*Institute of Multidisciplinary Research for Advanced Materials (IMRAM),
Tohoku University, Sendai, 980-8577, Japan*

¹⁰*CPHT, CNRS, Ecole Polytechnique,
Institut Polytechnique de Paris, F-91128 Palaiseau, France*

¹¹*Collège de France, 11 place Marcelin Berthelot, 75005 Paris, France*

¹²*Department of Physics, Division of Mathematical Physics,*

Lund University, Professorgatan 1, 22363 Lund, Sweden

¹³*Unité Mixte de Physique, CNRS, Thales, Université Paris-Sud,*

Université Paris-Saclay, 91767 Palaiseau, France

¹⁴*Université Paris-Saclay, CNRS, Laboratoire de Physique des Solides, Orsay 91405, France*

Abstract

In solids, strong repulsion between electrons can inhibit their movement and result in a “Mott” metal-to-insulator transition (MIT), a fundamental phenomenon whose understanding has remained a challenge for over 50 years. A key issue is how the wave-like itinerant electrons change into a localized-like state due to increased interactions. However, observing the MIT in terms of the energy- and momentum-resolved electronic structure of the system, the only direct way to probe both itinerant and localized states, has been elusive. Here we show, using angle-resolved photoemission spectroscopy (ARPES), that in V_2O_3 the temperature-induced MIT is characterized by the progressive disappearance of its itinerant conduction band, without any change in its energy-momentum dispersion, and the simultaneous shift to larger binding energies of a quasi-localized state initially located near the Fermi level.

According to the quantum-mechanical band theory of solids, in insulators the highest occupied band is totally filled, while in metals it is partially filled [1]. Thus, as temperature cannot change the number of electrons in a solid, it should not change either its intrinsic nature, i.e. metallic or insulating. Enter V_2O_3 : the formal configuration of the vanadium ion would be $V^{+3}[3d^2]$, hence this oxide should be a metal. However, bulk V_2O_3 shows a first-order metal-to-insulator transition (MIT) when cooling below $T_{MIT} \approx 160$ K, with an abrupt resistivity change of over six orders of magnitude [2–8] –see Figs. 1(A, B). Microscopically, the MIT is characterized by gap of about 750 meV opening in the optical conductivity [9, 10], and is accompanied by corundum-to-monoclinic and paramagnetic to antiferromagnetic transitions [4, 6, 7, 11, 12], as illustrated in Fig. 1(A). In fact, due to the relatively localized character of the $3d$ -orbitals, the partially-filled bands of V_2O_3 are prone to strong electronic correlations, neglected in band theory [2]. V_2O_3 is thus considered an archetypal system for the Mott MIT, one of the most fundamental manifestations of electron correlations, also observed in several other materials. However, after 50 years of research, the microscopic processes accompanying the Mott MIT, including the roles played by the electronic, magnetic and structural degrees of freedom, are still controversial issues [4, 6–9, 12–16]. A major reason is that an experimental imaging of the momentum-resolved changes in the electronic structure of any Mott system across the thermally induced MIT is still missing.

Previous photoemission experiments studied the momentum-integrated density of states of V_2O_3 , identifying a quasi-particle (QP) peak at the Fermi level (E_F) in the metallic phase [17] that disappears in the insulating state [18], and a broad feature at a binding energy $E - E_F \approx -1.1$ eV [19, 20], assigned to the lower Mott-Hubbard (MH) band [17, 18]. The coexistence of the QP peak and the MH band is the hallmark of the correlated state, as predicted by dynamical mean-field theory some 30 years ago [21]. More recently, ARPES experiments in the metallic phase of V_2O_3 single crystals [22] showed the existence of an electron-like QP band around the zone center (Γ point), dispersing down to about -400 meV over Fermi momenta $2k_F \approx 1 \text{ \AA}^{-1}$ along the ΓZ direction, and suggested the presence of a non-dispersive component of spectral weight in the metallic QP energy region.

However, several technical challenges have hindered the realization of momentum-dependent photoemission studies of the MIT in V_2O_3 . For instance, V_2O_3 crystals are extremely hard to cleave in order to expose a clean crystalline surface. Moreover, they become highly insulating below T_{MIT} , thus strongly charging upon electron emission, and break apart into pieces, due to the structural transition. The main physical issue at stake is at the core of the strong correlations problem, namely how electrons transmute from wave-like objects in the metallic phase to localized particles in the insulating one. In this work, we were able to directly address this question experimentally, and we provide answers to a variety of key questions: the evolution of the Mott gap, QP dispersions, effective masses, orbital character and relative spectral weights of the QP and Mott-Hubbard bands, and an understanding, from the viewpoint of electronic structure, of the hysteresis cycle observed in the MIT.

Using angle-resolved photoemission spectroscopy (ARPES), we studied high-quality crystalline thin films of V_2O_3 grown on Al_2O_3 substrates [23–25]. Thanks to the anchoring imposed by the latter, the crystal integrity of the films is not affected by stress due to the structural transition. This allowed us to measure, for the first time, the effects of the MIT on the *momentum-resolved* spectral function of the system. As schematized in Figs. 1(C-E), we found that the opening of the Mott gap at E_F in energy-momentum space happens *abruptly* following a gradual spectral-weight transfer: as temperature decreases in the MIT regime, there is a progressive decrease in spectral weight of an itinerant, i.e. dispersive quasi-particle (QP) conduction band, without noticeable changes in its dispersion and effective mass. This is accompanied by a shift, and increase in spectral weight, of a quasi-localized state (QLS),

which goes from an energy close to E_F in the metallic state to an energy close to the bottom of the vanishing dispersive band in the insulating state. Only when the dispersive state crossing the Fermi level has vanished a complete gap of about 700 meV with respect to E_F is observed, associated to the final energy position of the QLS. Furthermore, the spectral weight of the above-mentioned near- E_F features shows a clear thermal hysteresis that tracks the one observed in macroscopic transport data. Another non-dispersive state at lower binding energy, associated to the lower Mott-Hubbard (MH) band, and possibly also containing a contribution from oxygen vacancy (OV) states (see later), does not show an appreciable variation with temperature.

Fig. 2(A) shows the crystal structure of V_2O_3 both in its primitive high-temperature rhombohedral unit cell (blue) and in the associated conventional hexagonal cell (black). In rhombohedral coordinates of the primitive cell, we write as (hkl) the orientation of crystallographic planes, and as $\langle hkl \rangle$ directions in reciprocal space. In hexagonal coordinates of the conventional cell, we employ the four Miller indices notation, writing planes and directions respectively as $(hkil)$ and $\langle hkil \rangle$ (with $i = -h - k$).

In this work we measured $V_2O_3/Al_2O_3(11\bar{2}0)$ thin films, whose surface, schematically shown in Fig. 2(B), is perpendicular to the basal plane of the hexagonal cell. Complementary data on $V_2O_3/Al_2O_3(01\bar{1}2)$ films are presented in the Supplementary Information.

The surface of the V_2O_3 films was cleaned *in-situ* using protocols previously developed for the investigation of two-dimensional (2D) electron gases in oxides [26–30]. The cleaned surfaces showed well-defined low-energy electron diffraction (LEED) patterns (Supplementary Information). The cleaning process slightly lowers the onset temperature of the MIT and decreases the change in resistance between the insulating and metallic states, possibly due to the formation of oxygen vacancies [26, 27, 31, 32], but does not affect the stoichiometry of the film nor the overall physical changes across the transition (Supplementary Information). See the Methods for technical details about our thin-film growth, characterization, ultra-high-vacuum (UHV) annealing and ARPES measurements.

Fig. 2(C) shows the 3D rhombohedral Brillouin zone of V_2O_3 in its metallic phase, together with the 2D plane through Γ parallel to the surface of our films. For simplicity in notation, everywhere in this work the ARPES data will be referred to directions in this particular Brillouin zone, both in the metallic and insulating phases. When relevant, the Brillouin zone edges of the monoclinic insulating structure will be indicated. The sample's

surface orientation will be specified using hexagonal coordinates, as commonly done in the thin-film literature. The Supplementary Information discusses further the rhombohedral and monoclinic Brillouin zones in relation to our ARPES data in the metallic and insulating phases.

We now present the ARPES data across the MIT. Fig. 2(D) shows the Fermi surface map in the $(\bar{1}10)$ plane of a $V_2O_3/Al_2O_3(11\bar{2}0)$ thin film measured in the metallic state at $T = 180K$. One observes a large Fermi sheet around the center of the Brillouin zone (Γ point). Photon-energy-dependent ARPES data presented in the Supplementary Information (Fig. S5) show that the Fermi surface disperses in the momentum direction perpendicular to the sample surface, demonstrating that the measured states are intrinsic to the bulk three-dimensional electronic structure of the material. Fig. 2(E) presents the corresponding energy-momentum ARPES map along $k_{\langle 111 \rangle}$, corresponding to the ΓZ direction in the rhombohedral metallic phase. The most evident features are an electron-like QP band crossing the Fermi level ($E_F = 0$) and dispersing down to about -400 meV [18, 22], together with a non-dispersive state around an energy $E = -1.1$ eV, assigned to the lower MH band [18], and the valence band (VB) of oxygen p -states below about $E = -4$ eV. All these features are in excellent agreement with previous photoemission and ARPES measurements in the metallic state of single crystals [18, 22]. The clear dispersion of the QP and valence bands is, moreover, an experimental proof of the crystalline quality of the thin film surface. Note also that the Mott-Hubbard band has most of its spectral weight concentrated at momenta around Γ , below the QP band bottom, similarly to what has been previously seen in other correlated-electron metals [27, 33]. Part of the non-dispersive spectral weight present at the same energy as the MH band, also observed in previous ARPES works on V_2O_3 [22], might arise from localized states associated to the creation of oxygen vacancies during the annealing process and/or UV irradiation during experiments. Such vacancy states are commonly found at about the same binding energy, namely $E - E_F \approx -1$ to -1.5 eV, in virtually all transition metal oxides [26, 28, 29, 31, 32], including the correlated metal $SrVO_3$, where they indeed superpose with the MH band [27].

Thanks to our thin films that preserve their crystal integrity upon cooling, we can now measure the momentum-resolved spectra in the insulating phase. Fig. 2(F) shows the energy-momentum ARPES map along $k_{\langle 111 \rangle}$ at $T = 100$ K, in the insulating state of the $V_2O_3/Al_2O_3(11\bar{2}0)$ thin film. While the VB and the MH/OV bands remain essentially

unchanged, the states near E_F show a dramatic reconstruction: instead of the strongly dispersive QP state, one observes now a weakly dispersing, previously unreported quasi-localized state (QLS), at $E - E_F \approx -700$ meV, *different* from the MH/OV band. The energy of this QLS gives thus a lower bound to the Mott gap. This agrees well with the gap of about 750 – 800 meV observed in previous optical conductivity studies on V_2O_3 single crystals [9, 10]. It also agrees with our own infrared measurements on the same thin films used for our ARPES experiments, which show a strong decrease in reflectivity below about 800 – 900 meV in the insulating phase (Supplementary Information, Fig. S3). Note that optical measurements yield the true energy gap between the highest fully occupied state, hence the QLS, and the first unoccupied state above E_F , not accessible to ARPES. The QP, QLS, MH/OV and VB states can also be seen in the momentum-integrated ARPES intensities, Fig. 2(G). In fact, as we will see next, the QP and QLS states are *a priori* of different nature: the QLS is also present in the metallic phase at energies near E_F , where it coexists with the QP state –as hinted by previous ARPES work on the metallic phase of V_2O_3 single crystals [22]. But as the system becomes insulating, the QLS shifts down in energy and increases in intensity, while the QP state gradually loses its spectral weight.

Fig. 3 shows the detailed evolution of the near- E_F electronic structure, when the temperature is first gradually lowered from the metallic (180 K) to the insulating (60 K) state, panels (A-F) (curvature of intensity maps) and (L-Q) (raw data), then increased back to 180 K, panels (G-K) and (R-V). In the metallic state at $T \gtrsim 160$ K, Figs. 3(A, B) and (L, M), the QP band can be described by a free-electron-like parabola of effective mass $m^* \approx 3.5m_e$ (m_e is the free-electron mass), with its band bottom at $E_b \approx -400$ meV. The quasi-localized state, of weak intensity, can be better seen in the raw data around the Z points (near the edges of the energy-momentum maps, see also Figs. S7, S8, S9, Supplementary Information), beyond the Fermi momenta of the QP band. Its position, at $E - E_F \gtrsim -240$ meV, is indicated by the red markers in panels (L, M). The MH/OV state at $E - E_F \approx -1.1$ eV is also visible –black markers in panels (L, M). As the sample is cooled down and enters the transition regime at 130 K and 120 K, Figs. 3(C, D) and (N, O), the spectral weight of the QP band decreases, without any noticeable change in its effective mass (i.e., in its energy-momentum dispersion). Simultaneously, the QLS shifts down to $E \lesssim -400$ meV, becoming more intense as temperature is further lowered. In the insulating state at $T \lesssim 100$ K, Figs. 3(E, F) and (P, Q), the QP band has vanished. One observes only the weakly but clearly dispersing QLS

at $E - E_F \approx -700$ meV, which now shows a shallow band minimum at Γ and maxima at the monoclinic Brillouin zone edges (see also Fig. 2(F)), and the MH/OV band at $E \approx -1.1$ eV.

Upon heating up from the insulating state at 60 K back to the metallic state at 180 K, Figs. 3(F-K) and (Q-V), the spectral weight of the QLS decreases, rapidly shifting up in energy between 130 K and 160 K, while the dispersive QP band reappears. Strikingly, a clear *hysteresis* in the *thermal evolution* of the electronic states of the system is present, best seen in the transition regime around 120 K and 130 K –compare Figs. 3(C, D) to 3(I, H) and Figs. 3(N, O) to 3(T, S). Thus, in the cooling cycle, the QLS becomes more apparent (with respect the QP band) below 120 K, temperature at which the QP band is still visible. while in the heating cycle the QLS is clearly visible until 130 K, temperature at which the QP band only starts to re-emerge. The energy shift of the QLS also shows differences between the cooling and heating cycles, best seen when comparing the data at 130 K and 120 K. The Supplementary Information presents additional data and analyses of the thermal evolution of the near- E_F electronic structure measured in different samples.

The observation of a hysteresis in the ARPES spectra is related to the formation of phase-domains in the sample, an intrinsic characteristic of first-order phase transitions. Such domains, of micrometer to sub-micrometer size, have been directly imaged in real-space in VO_2 and V_2O_3 by near-field infrared microscopy [34, 35], photoemission microscopy [36] and muon spin-relaxation [37]. As the UV spot used in our experiments has a mean diameter larger than about 30 μm , the ARPES signal is a superposition of electrons emitted from both metallic and insulating phases. We then approximate the observed ARPES intensity $I(E, k, T)$ at a temperature T as a superposition of the intensity measured in the pure metallic phase ($T = 180$ K) at each energy E and wave-vector k and the intensity measured in the pure insulating phase ($T = 60$ K) at the *same* energy and momentum. In doing so we are assuming that, as suggested from Fig. 3, the energy shift of the QLS proceeds rather abruptly with temperature. We also neglect thermal broadening, as our energy resolution (of about 15 meV) is already comparable to $k_B T$ at 180 K. Thus, we write:

$$\begin{aligned}
 I(E, k, T) = & a(T) \times I(E, k, T = 180\text{K}) \\
 & + b(T) \times I(E, k, T = 60\text{K})
 \end{aligned}
 \tag{1}$$

Using linear regression, we could therefore determine the phase fractions $a(T) \geq 0$ and $b(T) \geq 0$ that best fit the measured spectra *for all energy and momenta*, i.e., over a set of

around 4×10^5 points of $I(k, E)$, at each temperature. Fig. 4(A) shows the so-calculated fraction of insulating and metallic domains, $b/(a+b)$ and $a/(a+b)$, as a function of temperature. For comparison, the resistance obtained on the same sample *after* ARPES measurements, Fig. 4(B), is also shown. The agreement in the hysteresis between the electrical resistance and the ARPES data (onset of the transition on cooling at around 140 – 150 K, mid-point at around 120 K, thermal amplitude of the hysteresis of about 15 – 20 K) indicates that the observed changes in the spectral function are directly linked to the metal-to-insulator transition.

Our temperature-dependent studies were performed along $k_{\langle 111 \rangle}$, a direction orthogonal to the antiferromagnetic wave-vector in the insulating state [11, 12]. Hence the band dispersions along this direction should not be directly affected by antiferromagnetic band folding. In line with this expectation, our ARPES data do not show any folding of the dispersive QP state. Instead, the spectral weight of the QP state vanishes as the system goes from metallic to insulating, without any measurable change in its dispersion, while the quasi-localized state shifts down in energy and increases in spectral weight. One possibility is that the energy shift of the QLS, which remains essentially non-dispersing along all high-symmetry directions explored in this work (Fig. 3 and Supplementary Information, Fig. S6), is associated to its nesting along momenta parallel to the antiferromagnetic wave-vector. On the other hand, note that in the insulating state the magnetic moments are ordered ferromagnetically along $k_{\langle 111 \rangle}$ [11]. This of course can affect the band structure, although in a way different from antiferromagnetic folding. Future theoretical studies should address further how the specific magnetic ordering of V_2O_3 affects its different orbital states.

More generally, our ARPES measurements show that, across the MIT, the essential redistribution of spectral weight in the occupied part of the electronic spectrum occurs between the QP and QLS bands, over an energy range of about 700 meV below E_F . On the other hand, recent optical measurements show that, while a large suppression of optical conductivity occurs indeed over an energy range of about 1 eV [38–40], a significant spectral weight transfer extends up to and beyond at least 3 eV [34, 39]. Thus, taken together, ARPES and optics data indicate that the unoccupied part of the electronic spectrum is also undergoing a major reconstruction, over a large energy range of several eV, across the MIT.

Our observations of spectral weight redistribution among the QP and QLS are consistent with X-ray absorption spectroscopy measurements, which found that the metallic

and insulating phases have different orbital occupancies among two states present in both phases [41, 42]. Our findings are also in line with multi-orbital first-principles calculations for V_2O_3 [14, 43, 44]. In the metallic phase, the dispersive quasi-particle band seen in the ARPES spectra and crossing the Fermi level is identified in the calculations as a band of a_{1g} dominant character, while the remaining spectral weight stems essentially from the e_g^π orbitals. In particular, the latter would be mainly responsible for the spectral weight of the broad quasi-localized state around E_F , as well as the Hubbard band feature around -1.1 eV. In the insulating phase, the dispersive a_{1g} band would be emptied, and only the double peak structure (at energies -0.7 eV and -1.1 eV) of the Hubbard band formed by the now half-filled e_g^π -states would survive [14, 43, 45]. Our data provides thus a direct, momentum-resolved illustration of the multi-orbital nature of the Mott transition in V_2O_3 .

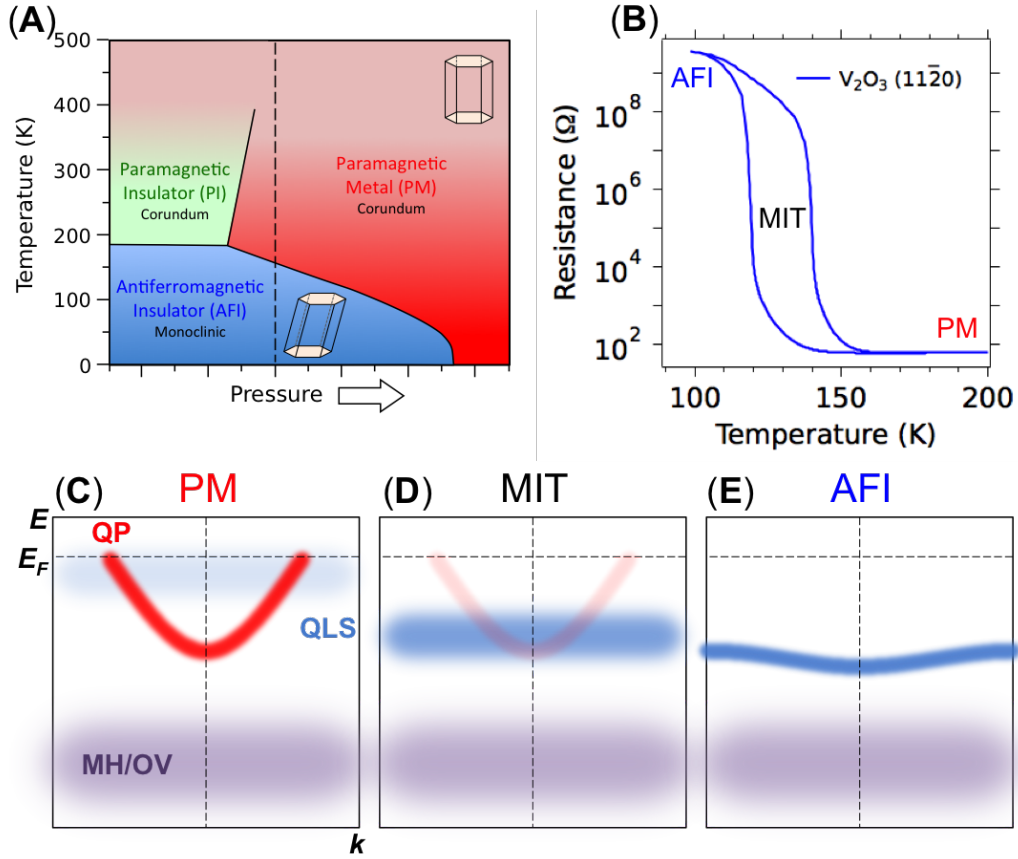


Figure 1. **V_2O_3 : schematic phase diagram and electronic-structure changes.** (A) Generic temperature-pressure phase diagram of bulk V_2O_3 [5]. (B) Electrical resistance of a $V_2O_3/Al_2O_3(11\bar{2}0)$ thin film studied in this work, showing the paramagnetic metal (PM), antiferromagnetic insulator (AFI), and the coexistence region across the MIT. (C, D, E) Schematic representation of the near- E_F electronic-structure evolution observed in this work. In the PM phase, a QP band and a QLS are observed near E_F . In the coexistence region, the QP loses spectral weight without changes in dispersion, while the QLS shifts down in energy and gains spectral weight. In the AFI phase, only the QLS (showing a slight dispersion) remains, resulting in a gap below E_F .

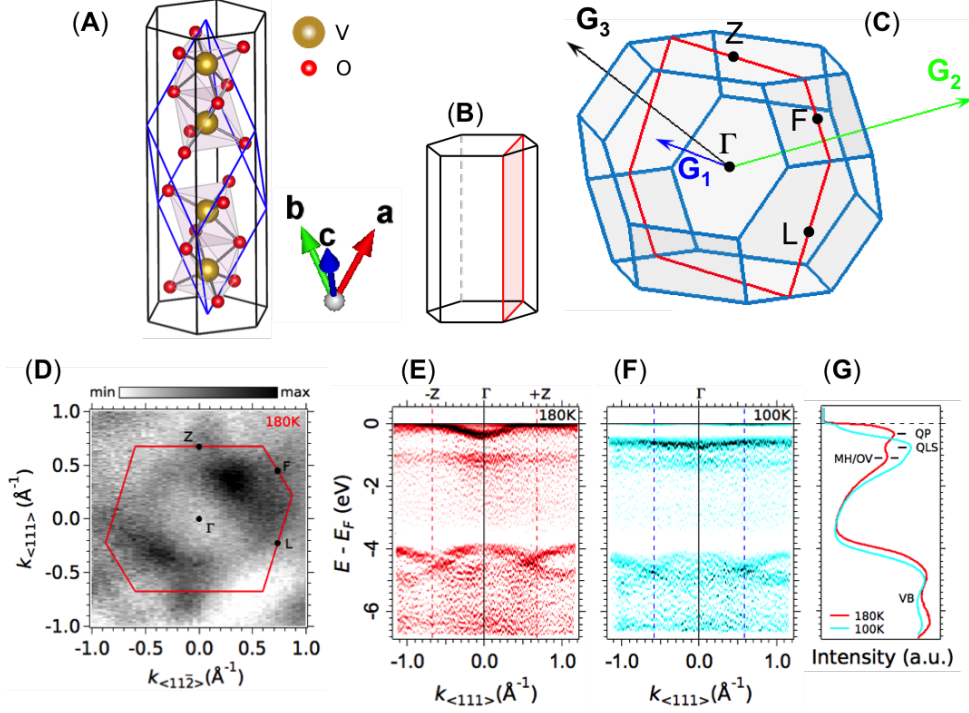


Figure 2. **V₂O₃: Crystal structure and electronic gap opening across the MIT.** (A) Rhombohedral crystal structure of V₂O₃ (blue polyhedron) in the high-temperature metallic state. The non-primitive hexagonal cell (black polyhedron) is also shown. (B) Representation of the (11 $\bar{2}$ 0) plane (in red) measured in this work inside the non-primitive hexagonal cell. (C) Rhombohedral Brillouin zone, showing the primitive vectors of the reciprocal lattice. The ($\bar{1}$ 10) plane, corresponding to a (11 $\bar{2}$ 0) plane in hexagonal coordinates, is shown in red. (D) Fermi-surface map in the $\langle 111 \rangle - \langle 11\bar{2} \rangle$ plane of a thin film of V₂O₃/Al₂O₃(11 $\bar{2}$ 0) in the metallic state at 180 K. The rhombohedral Brillouin zone edges are marked in red. Associated high-symmetry points are indicated. (E, F) Energy-momentum maps (2D curvature) along ΓZ in the metallic (180 K) and insulating (100 K) states, respectively, showing four bands: an electron-like QP band at the Fermi-level, visible at 180 K; a weakly dispersive QLS at $E - E_F \approx -700$ meV, best observed at 100 K; a broad and weakly dispersing MH/OV band around $E - E_F \approx -1.1$ eV, seen at both temperatures; and the VB of oxygen *p*-states extending from $E - E_F \approx -4$ eV downwards, also present at all temperatures. The rhombohedral Brillouin zone edges ($\pm Z$) at 180 K, and the monoclinic zone edges at 100 K, are indicated by red and blue dashed lines, respectively. (G) Momentum-integrated raw ARPES intensities from (E) and (F), showing the QP, QLS, MH/OV and VB states. All data were measured at a photon energy of 86 eV, corresponding to a bulk Γ point in the $\langle \bar{1}10 \rangle$ direction, using linear horizontal polarized light. The color hues in panels (D, E,F), as in the rest of this paper, indicate the ARPES intensity between the minimum (min) and maximum (max) detected signal. See the Methods for a detailed description of the ARPES measurements and curvature analyses.

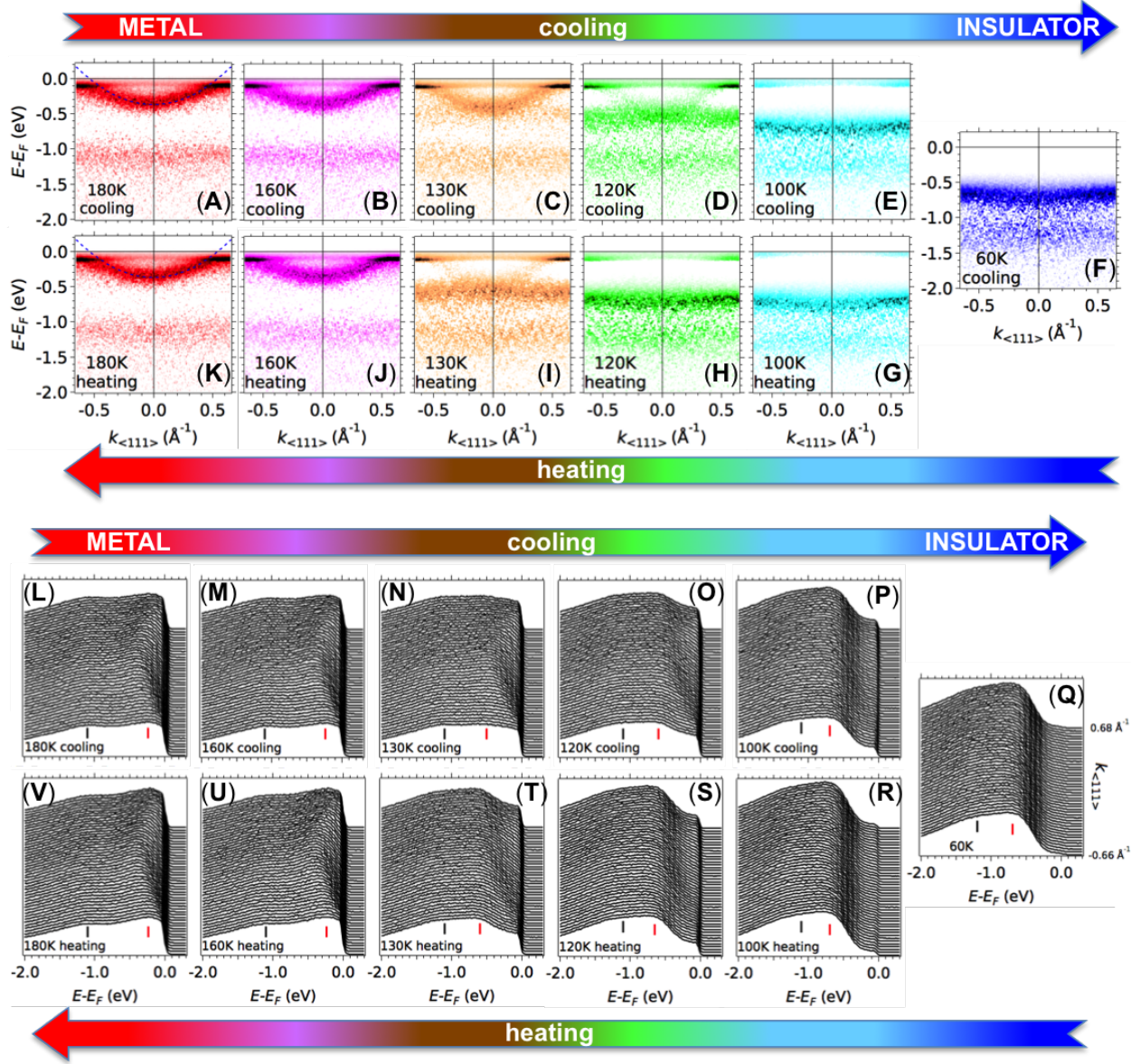


Figure 3. **Reconstruction and hysteresis of the electronic structure across the MIT.** (A-F) Evolution of the ARPES energy-momentum spectra near E_F (2D curvature of intensity maps, see Methods) when cooling from 180 K (metallic state) to 60 K (insulating state) in a $V_2O_3(1\ 1\ \bar{2}0)$ thin film. The sharp pile-up of intensity at E_F is a spurious effect of the 2D curvature analysis on the Fermi-Dirac cutoff. (G-K) Corresponding spectra when heating back to 180K. The blue dashed parabolas in (A) and (K) represent a quasi-free electron band of effective mass $m^* = 3.5m_e$, assigned to the QP band. (L-V) Raw data associated to (A-K). Red and black markers indicate the positions of the QLS and MH/OV bands, respectively.

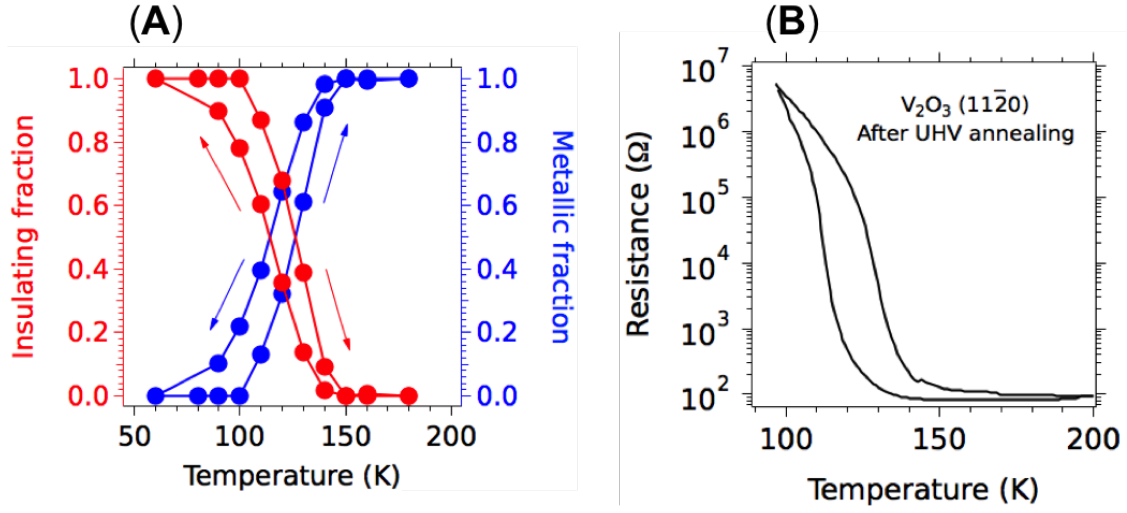


Figure 4. **Fraction of metallic and insulating electronic domains from ARPES.** (A) Representation of the fraction of insulating and metallic domains contributing to the ARPES intensity in a $V_2O_3/Al_2O_3(11\bar{2}0)$ thin film. Error bars in the fits, Eq. 1, are smaller than the size of the symbols. (b) Resistance as a function of temperature measured in the same sample *after* UHV annealing and photoemission experiments. The shift in transition temperature and the decrease of the resistivity in the insulating phase with respect to the pristine sample, Fig. 1(C), are ascribed to the slight doping with oxygen vacancies induced by annealing in UHV (Supplementary Information).

METHODS

Thin-film growth and characterization

The 100 nm thick epitaxial V_2O_3 thin films were deposited on $(1\ 1\ \bar{2}\ 0)$ or $(0\ 1\ \bar{1}\ 2)$ oriented Al_2O_3 substrates by RF magnetron sputtering, as described in a previous work [25]. An approximately 8 mTorr ultra high purity Argon ($> 99.999\%$) and the growth temperature of $700^\circ C$ were used during the sputtering process. The thin film structural properties were measured using a Rigaku SmartLab x-ray diffraction system. Resistance vs temperature measurements were done using a TTPX Lakeshore cryogenic probe station equipped with a Keithley 6221 current source and a Keithley 2182A nanovoltmeter.

Crystal structure and Brillouin zone of V_2O_3

In the high-temperature metallic phase, bulk V_2O_3 crystallizes in a rhombohedral (corundum) structure, as shown in Fig. 1(B), with lattice parameters $|\mathbf{a}| = |\mathbf{b}| = |\mathbf{c}| = 5.467\ \text{\AA}$ and angles between lattice vectors $\alpha = \beta = \gamma = 53.74^\circ$. Such a structure can be equally represented in a non-primitive hexagonal cell, also shown in Figs. 1(B, C). The Miller indices (h_R, k_R, l_R) in rhombohedral coordinates are related to the Miller indices $(h_H, k_H, i_H = -h_H - k_H, l_H)$ in the corresponding hexagonal coordinates by:

$$\begin{aligned} h_R &= \frac{1}{3}(-k_H + i_H + l_H) \\ k_R &= \frac{1}{3}(h_H - i_H + l_H) \\ l_R &= \frac{1}{3}(-h_H + k_H + l_H) \end{aligned}$$

Our thin films are grown on $Al_2O_3(1\ 1\ \bar{2}\ 0)$ (a-plane) and $Al_2O_3(0\ 1\ \bar{1}\ 2)$ (R-plane) surfaces, corresponding respectively to the $(\bar{1}\ 1\ 0)$ and $(0\ 1\ 1)$ planes in rhombohedral coordinates. Thin films grown on different Al_2O_3 surfaces present a slight distortion (at most 1% of strain) from the ideal corundum symmetry [25], which is negligible for ARPES measurements. Hence, in this work, we use the bulk primitive rhombohedral Brillouin zone to represent the ARPES data.

ARPES measurements

ARPES experiments were performed at the CASSIOPEE beamline of Synchrotron SOLEIL (France) and at beamline 2A of KEK-Photon Factory (KEK-PF, Japan) using hemispherical electron analyzers with vertical and horizontal slits, respectively. Typical electron energy and angular resolutions were 15 meV and 0.25° . In order to generate pristine surfaces for the ARPES experiments, the thin films of V_2O_3 were annealed for 5-10 minutes at approximately 550-600°C in UHV conditions, at a base pressure of 10^{-9} mbar before annealing, reaching a desorption peak of $\approx 8 \times 10^{-7}$ mbar during annealing. Low-energy electron diffraction (LEED) was employed to verify the long-range crystallinity and cleanliness of our surfaces after preparation –see Supplementary Information, Fig. S1.

While the insulating phase of V_2O_3 would prevent the realization of ARPES experiments on a bulk sample, we found that the residual conductivity in our samples was enough to reduce the charging of the film to approximately 11 eV at 100K under the photon flux used for our measurements. The charging was subsequently corrected by aligning the energy of the Fermi-Dirac steps (if a residual spectral weight at E_F was present) or of the valence bands at all temperatures, thus assuming that such a band is not affected by the MIT. Such a hypothesis is not only physically sound, given the high binding energy of the O-2p levels that form the VB and their large separation from the MH and QP bands, but is also supported by the data which, apart from the expected thermal broadening and energy shift due to charging, do not show any significant changes in the valence band shape when the system is cooled/warmed across the MIT.

Second derivative rendering of ARPES intensity maps

For second derivative rendering (Supplementary Information, Fig. S5(C)) the raw photoemission energy-momentum maps were convolved with a two-dimensional Gaussian of FWHM's 2° in angle and 25 meV in energy in order to smooth the noise. Only negative values of the second derivative, representing peak maxima in the original data, are shown.

2D curvature rendering of ARPES intensity maps

The 2D curvature method [46] was used to enhance the intensity of broad/weak spectral features in the ARPES intensity maps. To this end, boxcar smoothing was applied to the raw data. For Figs. 2(B, C), we used a kernel of $80 \text{ meV} \times 0.037 \text{ \AA}^{-1}$ with a 2D curvature free parameter of 0.2. For Figs. 3(A-K), we used a kernel of $140 \text{ meV} \times 0.026 \text{ \AA}^{-1}$ with a 2D curvature free parameter of 0.1. Only negative values of the 2D curvature, which represent maxima in the original data, are shown. After taking the 2D curvature, the data were rigidly shifted by 30 meV towards the Fermi level, in order to preserve the exact peak positions as determined by the raw data and its second derivatives. There is no effect on the conclusions of this study as an identical shift was applied to all figures where the 2D curvature rendering is displayed.

3D k -space mapping

Within the free-electron final state model, ARPES measurements at constant photon energy give the electronic structure at the surface of a spherical cap of radius $k = \sqrt{\frac{2m_e}{\hbar^2} (h\nu - \Phi + V_0)^{1/2}}$. Here, m_e is the free electron mass, Φ is the work function, and $V_0 = 12.5 \text{ eV}$ is the “inner potential” of V_2O_3 [22]. Measurements around normal emission provide the electronic structure in a plane nearly parallel to the surface plane. Likewise, measurements as a function of photon energy provide the electronic structure in a plane perpendicular to the surface.

Thermal cycling in ARPES measurements

In order to accurately capture the electronic hysteresis behavior across the MIT, the samples were loaded into the ARPES manipulator at 200K. Once thermalized, we performed a slow stepwise cooling cycle, setting the parameters in the temperature controller so as to avoid overshooting the desired new temperature (hence avoiding spurious hysteresis cycles), then letting the system thoroughly thermalize at that temperature for over 30 minutes before measuring. After reaching the lowest measurement temperature, we performed an analogous heating cycle, measuring at the same temperatures as during the cooling cycle.

Acknowledgments

We thank François Bertran for assistance during ARPES measurements at CASSIOPEE (Synchrotron SOLEIL). Work at ISMO was supported by public grants from the French National Research Agency (ANR), project Fermi-NES_t No. ANR-16-CE92-0018, the “Laboratoire d’Excellence Physique Atomes Lumière Matière” (LabEx PALM projects ELECTROX, 2DEG2USE and 2DTROX) overseen by the ANR as part of the “Investissements d’Avenir” program (reference: ANR-10-LABX-0039), and the CNRS International Research Project EXCELSIOR. Work at KEK-PF was supported by Grants-in-Aid for Scientific Research (Nos. 16H02115 and 16KK0107) from the Japan Society for the Promotion of Science (JSPS). Experiments at KEK-PF were performed under the approval of the Program Advisory Committee (Proposals 2016G621 and 2018S2-004) at the Institute of Materials Structure Science at KEK. Work at UCSD was supported by the Air Force Office of Scientific Research under award number FA9550-20-1-0242. R. L. B. was supported by NWO through a VICI grant. P. H. R.-G. was supported by a CAPES grant, Brazil.

Author contributions

Project conception: A.F.S.-S., M.J.R., J.T. and I.K.S.; ARPES measurements: M.T, R.L.B., P.H.R.-G., E.D., E.F., F.F., P.L.F., K.H., H.K, and A.F.S.-S; sample growth, structural characterization and transport measurements: M.-H.L., N.M.V., Y.K., under the supervision of I.K.S; infrared measurements: A.Z.; data analysis and interpretation: M.T, E.F and A.F.S.-S, with input from M.J.R. and S.B.; writing of the manuscript: M.T. and A.F.S.-S. This is a highly collaborative research. All authors discussed extensively the results, interpretation and manuscript.

Competing interests

Authors declare that they have no competing financial interests.

Data availability

All data needed to evaluate the conclusions of this work are present in the paper and/or the Supplementary Information.

Additional information

Correspondence and requests for materials should be addressed to A.F.S.-S. (e-mail: andres.santander-syro@universite-paris-saclay.fr).

SUPPLEMENTARY INFORMATION

Low-energy electron diffraction (LEED)

(A) $V_2O_3/Al_2O_3(01\bar{1}2)$ (B) $V_2O_3/Al_2O_3(11\bar{2}0)$

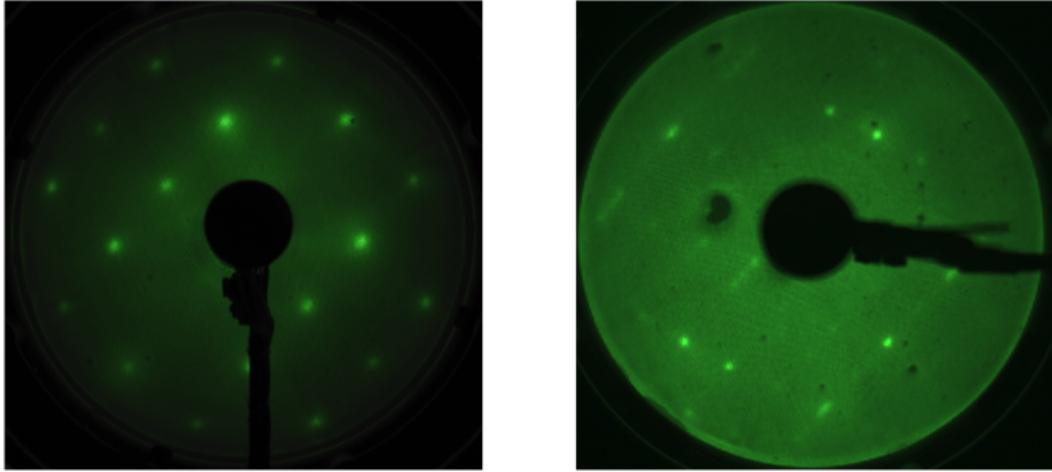


Figure S1. **LEED images of the studied V_2O_3 thin film surfaces.** (A, B) LEED images of $V_2O_3/Al_2O_3(01\bar{1}2)$ and $V_2O_3/Al_2O_3(11\bar{2}0)$ films, respectively, obtained after in-situ annealing, right before ARPES measurements.

Figure S1 shows the LEED images of our $V_2O_3/Al_2O_3(01\bar{1}2)$ and $V_2O_3/Al_2O_3(11\bar{2}0)$ thin films obtained after in-situ annealing. The periodically arranged sharp spots indicate a clean, crystalline surface, suitable for ARPES measurements.

Effects of in-situ annealing on the V_2O_3 thin films

Fig. S2 presents the X-ray diffraction (XRD) and electrical resistance characterizations of our $V_2O_3/Al_2O_3(01\bar{1}2)$ and $V_2O_3/Al_2O_3(11\bar{2}0)$ thin films before (blue or green curves) and after (red or yellow curves) the annealing in UHV required for ARPES experiments. Note that XRD is a bulk-sensitive measurement probing the entire thickness of the V_2O_3 film, while temperature-dependent electrical transport properties are very sensitive to changes in surface oxygen stoichiometry. Accordingly, no significant changes in crystal structure (main peaks of the XRD diagrams), hence in the bulk stoichiometry of the film, are observed. On the other hand, the onset of the resistive MIT on cooling is shifted down in temperature

from $\approx 160\text{K}$ to $\approx 140\text{ K}$ in the $\text{V}_2\text{O}_3/\text{Al}_2\text{O}_3(01\bar{1}2)$ film, and from $\approx 140\text{ K}$ to $\approx 130\text{ K}$ in the $\text{V}_2\text{O}_3/\text{Al}_2\text{O}_3(11\bar{2}0)$ film, while the change in resistance between the insulating and metallic phases is reduced by about three orders of magnitude in both films.

We ascribe the observed changes after UHV annealing to the creation of oxygen vacancies, a phenomenon well known and reported in many other transition metal oxides [26, 28–32], including other correlated-electron vanadium oxides such as SrVO_3 [27]. Indeed, in many of these oxides oxygen vacancies act as electron donors [26–32]. The important fact, however, is that the MIT and its hysteresis cycle are preserved, as indeed attested by the ARPES data, the latter being in very good agreement with the resistivity hysteresis cycle after UHV annealing. Such slight metallization of the sample is beneficial for the ARPES measurements, as it allows following the MIT without excessive charging down to the insulating state.

The previous is confirmed by infrared spectroscopy measurements, Fig. S3. These show that, in the metallic phase, the low-energy (far infrared) reflectivity, related to the concentration of free carriers in the sample, is slightly lower in a pristine $\text{V}_2\text{O}_3/\text{Al}_2\text{O}_3(01\bar{1}2)$ sample compared to a sample of the same batch that was annealed then measured by ARPES. Note that, in the insulating phase, the reflectivity of both samples strongly decreases at energies below about $800 - 900\text{ meV}$, showing thus that the optical gap in our thin films is similar to the one measured in single crystals, and is not appreciably affected by the UHV annealing. The only appreciable effect of UHV annealing, in phase with our characterizations from resistivity measurements, is that the temperature-dependent change in reflectivity at, e.g., 370 meV (inside the energy gap), is shifted down by about 15 K in the annealed sample.

Rhombohedral and monoclinic Brillouin zones of V_2O_3

Figure S4 compares the rhombohedral and monoclinic Brillouin zones in the metallic and insulating phases of V_2O_3 , respectively. While the two Brillouin zones are quite different in 3D reciprocal space, our temperature-dependent data were all measured in a fixed direction (in the laboratory frame of reference) coinciding with the rhombohedral ΓZ direction. Along this direction, the distance from Γ to the Brillouin zone edge is reduced only by about 0.09 \AA^{-1} in the monoclinic phase (i.e., a reduction of about 13% with respect the rhombohedral ΓZ distance). This value is comparable to our experimental resolution in momentum. Thus, for simplicity in notation, we choose to refer all momentum directions

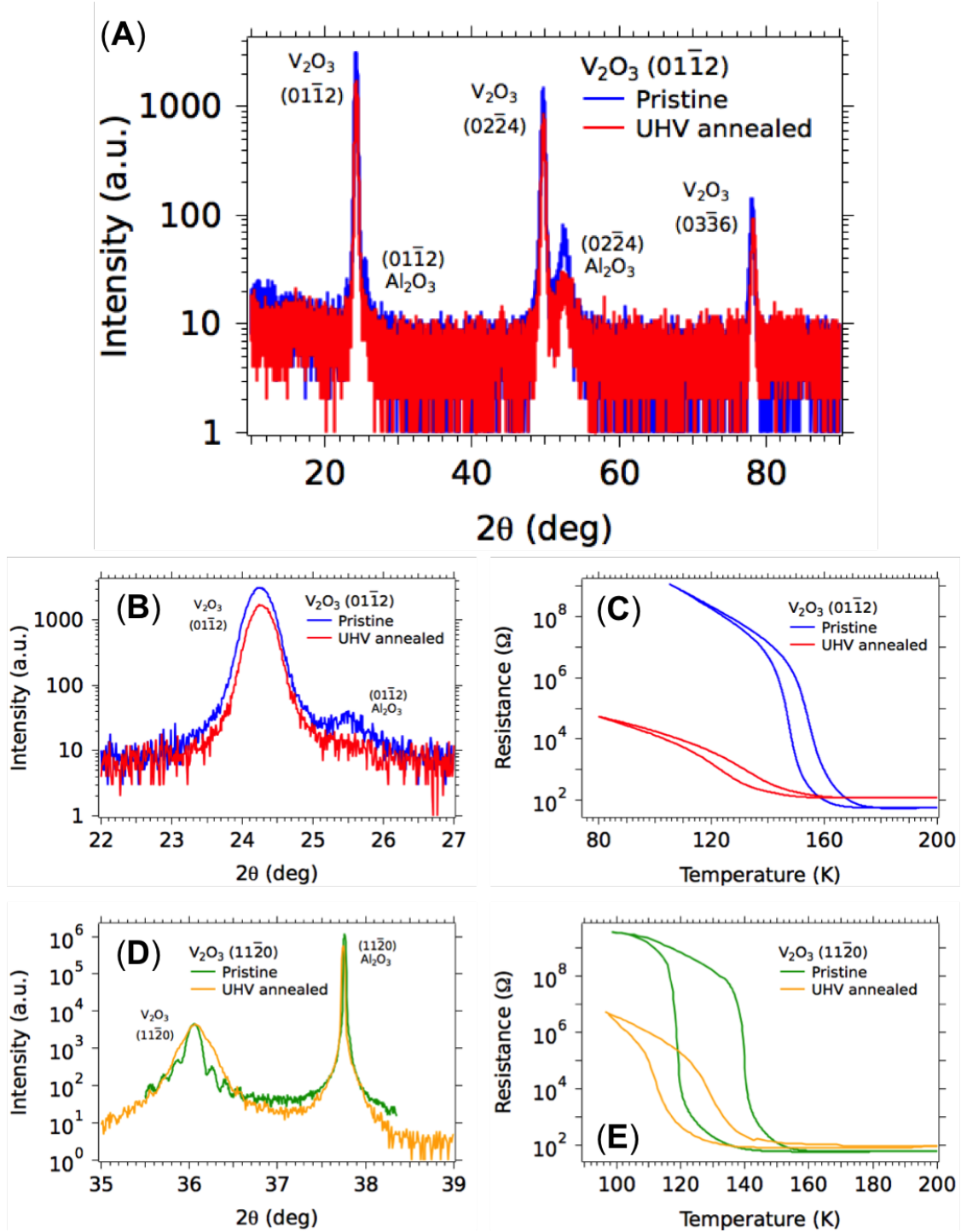


Figure S2. X-ray and resistance characterizations of the V_2O_3 films. (A, B) X-ray diffraction characterization, and (C) resistance measurements on a $V_2O_3/Al_2O_3(01\bar{1}2)$ thin film used in some of our ARPES experiments (see Fig. S11 below), before (blue) and after (red) the in-situ annealing in UHV. Panel (B) is a zoom over the V_2O_3 and $Al_2O_3(01\bar{1}2)$ peaks. (D, E) Analogous measurements to (B, C) on the $V_2O_3/Al_2O_3(11\bar{2}0)$ thin films used in our ARPES experiments, before (green) and after (yellow) the in-situ annealing in UHV.

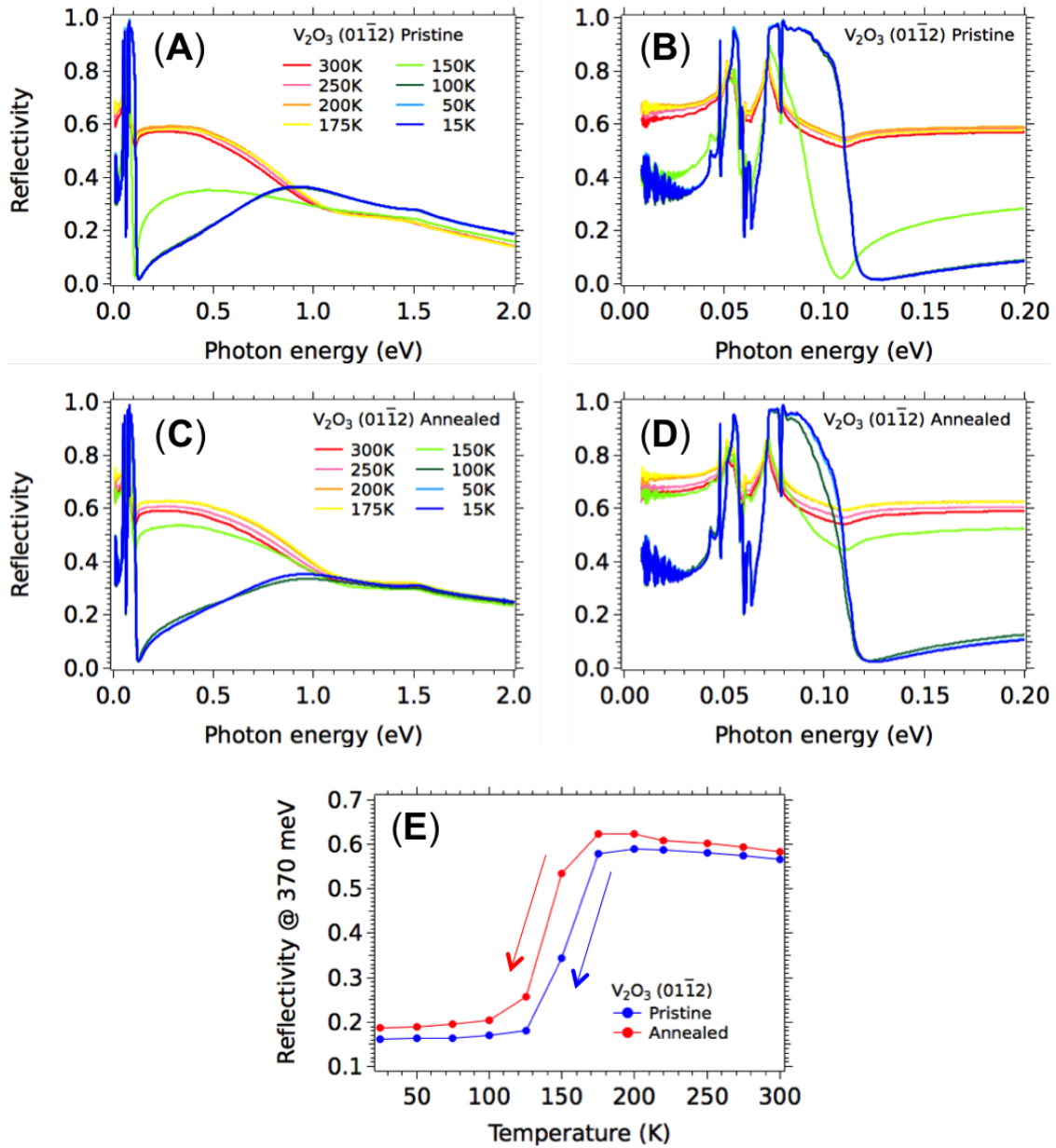


Figure S3. **Infrared reflectivity characterization of the V_2O_3 films.** (A) Infrared reflectivity measurements for various temperatures (cooling cycle) in a pristine $V_2O_3/Al_2O_3(01\bar{1}2)$ thin film. (B) Zoom of the previous data over the low-energy excitations. (C, D) Similar to (A, B) on a sample of the same batch that was annealed in UHV prior to ARPES measurements. (E) Reflectivity at 370 meV as a function of temperature for both samples. All these data show that the MIT is still present in the annealed sample studied by ARPES, and the onset of the transition has just shifted down in temperature by about 15 K.

in our ARPES data to the rhombohedral “frame of reference”. When pertinent in a given figure, the monoclinic zone edges for the energy-momentum maps in the insulating state are

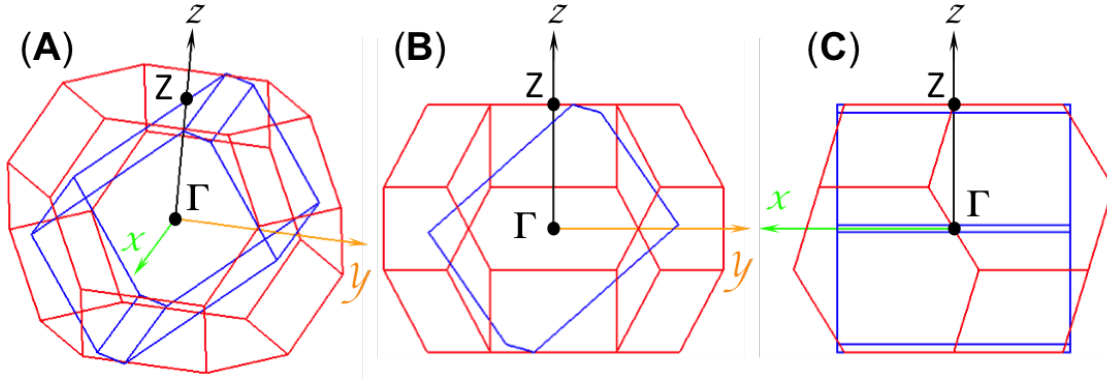


Figure S4. **Rhombohedral and monoclinic Brillouin zones of V_2O_3 .** (A) Comparison between the rhombohedral (red) and monoclinic (blue) Brillouin zones of V_2O_3 , corresponding respectively to the metallic and insulating phases. The xyz axes are also shown. (B, C) Same as (A) viewed from the x -side and y -side, respectively.

also shown.

In-plane and out-of-plane Fermi surfaces

Figure S5 shows the in-plane and out-of-plane Fermi surfaces measured at 180 K for the same $V_2O_3/Al_2O_3(1\bar{1}\bar{2}0)$ studied in the main text, together with the experimentally determined Fermi momenta. The out-of-plane dispersion in the Fermi surface corroborates the 3D nature of the measured state, as 2D surface states would not disperse in the momentum direction perpendicular to the surface. The main feature of the observed Fermi surface is a large electron-like sheet centered at Γ -however open in the direction ΓL , as will be seen next.

Raw ARPES energy-momentum maps

Figure S6(A) shows the $\Gamma - L - Z - \Gamma - F - Z$ path in reciprocal space, and Figs. S6(B, C) show the ARPES energy-momentum maps in the metallic phase along such a path. One observes that the QP state has an electron-like dispersion along ΓZ and ΓF , while along ΓL the state appears broad and, within resolution, non dispersive -such that this Fermi surface sheet would be open around the L points. The state shows a hole-like dispersion along LZ ,

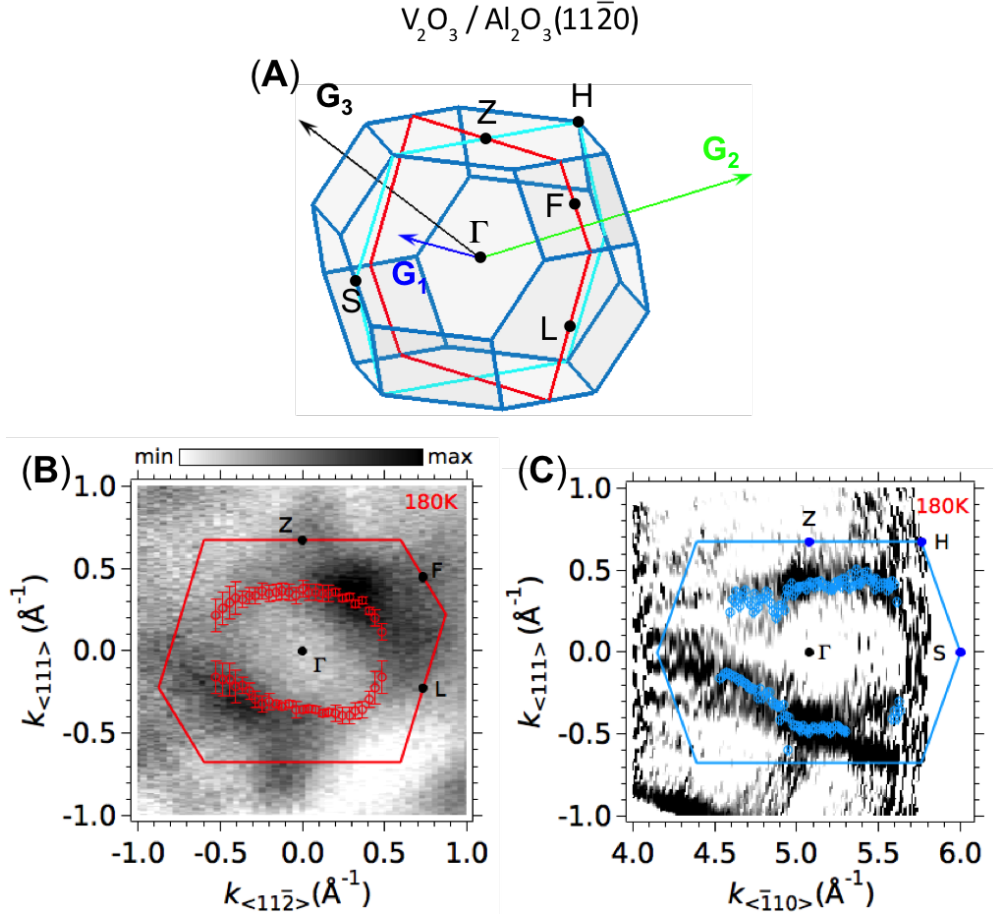


Figure S5. **In-plane and out-of-plane Fermi surfaces in the metallic state of V_2O_3 .** (A) Rhombohedral 3D Brillouin zone of V_2O_3 , showing the primitive vectors of the reciprocal lattice, together with a $(\bar{1}10)$ plane (red) and a $(11\bar{2})$ plane (light blue). These planes are, respectively, parallel and perpendicular to the surface of the studied $\text{V}_2\text{O}_3/\text{Al}_2\text{O}_3(11\bar{2}0)$ films. (B) Same in-plane Fermi-surface map (metallic state at 180 K) of a $\text{V}_2\text{O}_3/\text{Al}_2\text{O}_3(11\bar{2}0)$ sample shown in the main text. Red open markers show the experimental Fermi momenta with their respective error bars. Data were measured at $h\nu = 86$ eV (c) Out-of-plane Fermi-surface map (2D curvature, see Methods) of the same sample. Blue open markers show the experimental Fermi momenta with their respective error bars. Data were acquired by varying the photon energy between 55 eV and 120 eV in steps of 0.5 eV using linear horizontal polarized light.

such that around Z one has a hole-like Fermi pocket. The QLS can be observed as a weak, broad, non-dispersive part of spectral weight near E_F at all momenta, and is more visible around Z and along ZFZ. Additional data for the QLS, and its thermal evolution, will be discussed in the next section.

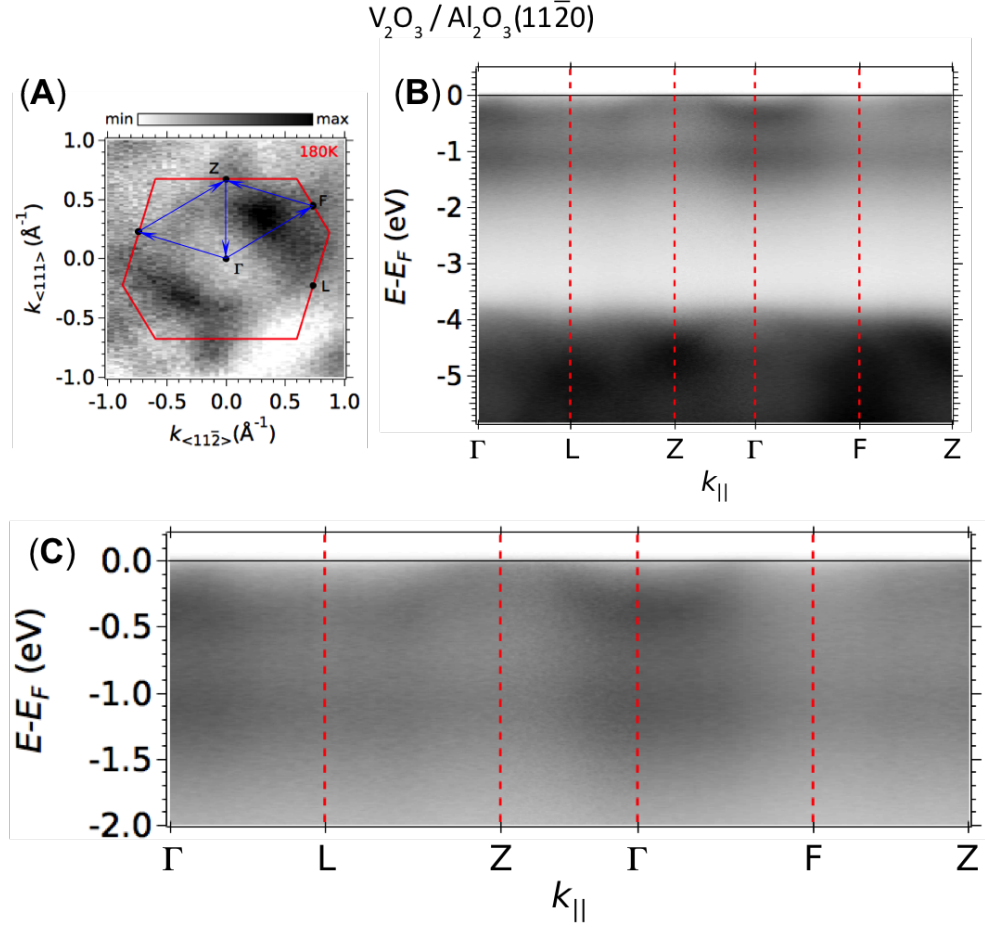


Figure S6. **Raw ARPES energy-momentum maps in the metallic state of V_2O_3 .** (A) Same in-plane Fermi-surface map as shown in previous figures indicating the path in reciprocal space for the raw ARPES energy-momentum maps in the metallic state (180 K) presented in panels (B, C). Data in (B) include the VB-top, MH/OV, QP and QLS bands. Panel (C) is a zoom of (B) over the MH/OV, QP and QLS features.

Figures S7(A-C) show, respectively, the raw energy-momentum ARPES maps along ΓZ , or $k_{\langle 111 \rangle}$, at 180 K and 100 K, and the integrated ARPES intensity of the previous two, corresponding to the same samples and data presented in Fig. 2 of the main text. At 180 K, the QP, MH/OV and VB are clearly visible. The weak non-dispersive QLS is also seen right below E_F in Fig. S7(A), spanning all the momenta within the measurement window. At 100 K, the QP band has vanished, and only the QLS, MH/OV, and VB are observed.

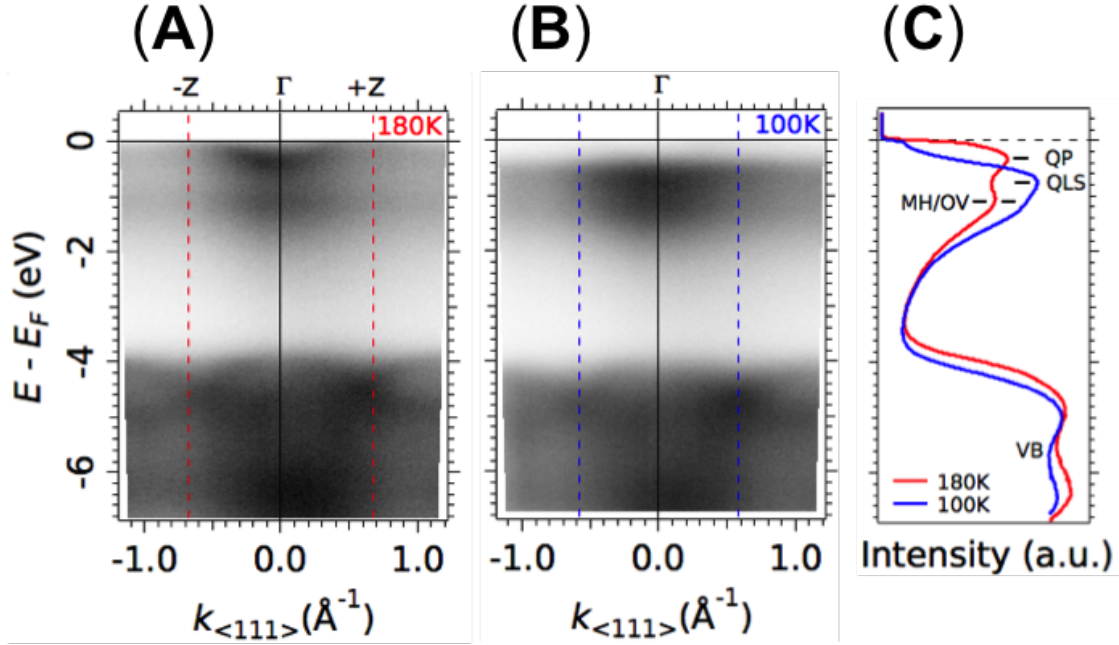
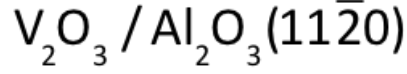


Figure S7. **Raw ARPES energy-momentum maps in the metallic and insulating states of V_2O_3 .** (A, B) Raw ARPES energy-momentum maps along ΓZ (or $k_{\langle 111 \rangle}$) over a wide energy range in the metallic (180 K) and insulating (100 K) states respectively, corresponding to the 2D curvature images shown in Figs. 2(B, C) of the main text. The rhombohedral Brillouin zone edges ($\pm Z$ points) at 180 K, and the monoclinic zone edges at 100 K, are indicated by red and blue dashed lines, respectively. (C) Corresponding momentum-integrated ARPES intensities showing the QP, QLS, MH/OV and VB states, identical to Figs. 2(D) of the main text, displayed again here for completeness. All data in this figure were measured at a photon energy of 86 eV, corresponding to a bulk Γ point in the out-of-plane direction, using linear horizontal light polarization.

Detailed temperature evolution of the quasi-localized state

In the metallic phase at high temperatures, the quasi-localized state is best observed at momenta where it does not overlap with the intense dispersing QP state, such as the edges of the Brillouin zone –where the QP peak is located at energies above E_F . Figures S8(A, B) compare the energy distribution curves (EDCs) at the Γ (zone center) and $\pm Z$ (zone edges) points over, respectively, a cooling and heating cycle across the MIT. Figures S8(C, D)

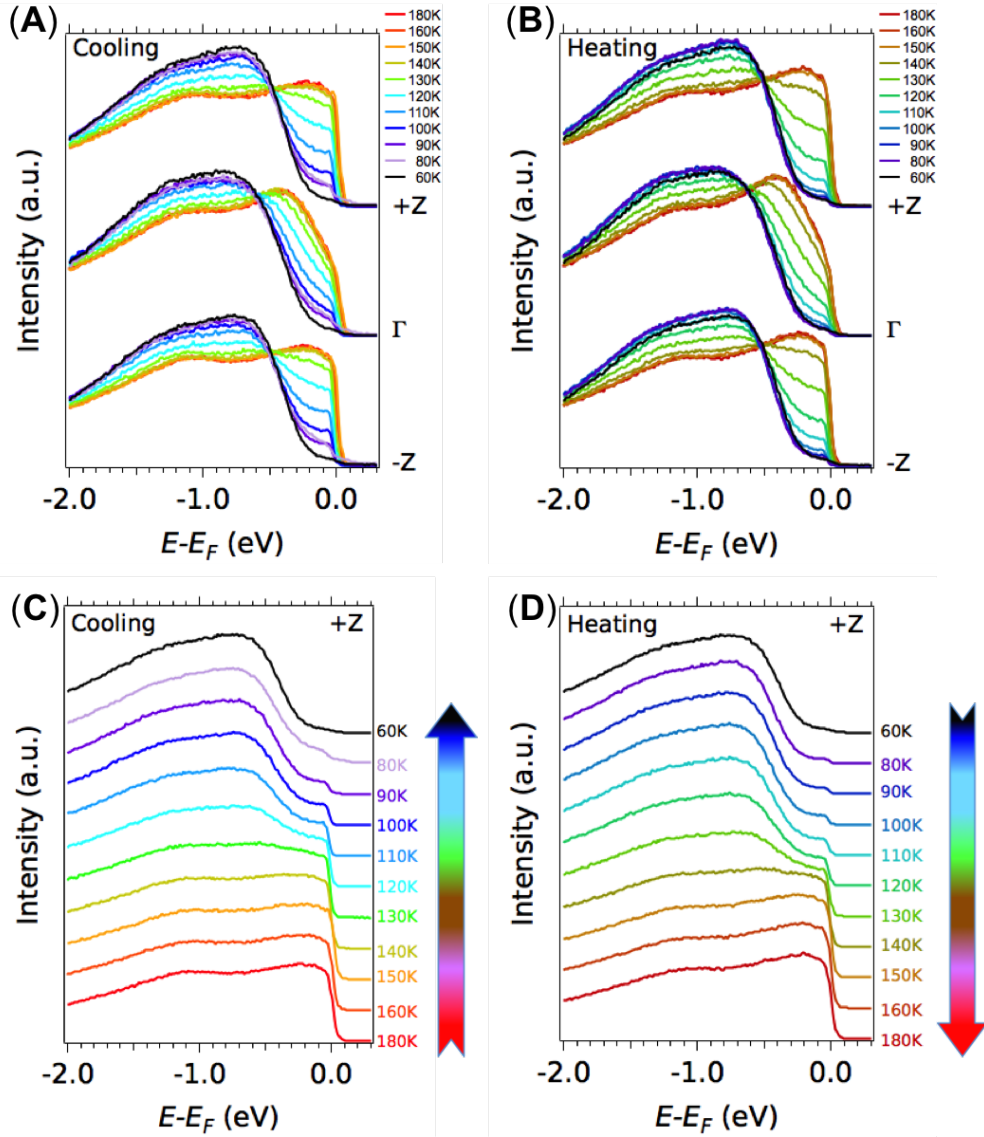
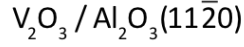


Figure S8. **Temperature evolution of the spectra at Γ and $\pm Z$.** (A, B) Energy distribution curves (EDCs) at Γ and $\pm Z$ (integrated over 0.03 \AA^{-1} around each point) over, respectively, a cooling and a heating cycle across the MIT. (C, dD Thermal evolution (cooling and heating) of the EDCs only at the $+Z$ point. All data in this figure correspond to the spectra shown in Fig. 3 of the main text, including additional temperatures, for a $\text{V}_2\text{O}_3(11\bar{2}0)$ thin film. Spectra at the same temperature on opposite thermal cycles are shown in slightly different color hues, for clarity.

show the temperature evolution (cooling and heating) of the EDCs only at the $+Z$ point. The data correspond to the spectra shown in Fig. 3 of the main text, including additional

temperatures. At 180 K, the broad peak of the QLS around $E - E_F \approx -240$ meV can be clearly observed at the zone edges. Note that thermal plus resolution broadening of the Fermi-Dirac cutoff occur on a smaller energy scale, of about 20 meV around E_F , so the peak at $E - E_F \approx -240$ meV corresponds to an intrinsic spectral feature. As temperature decreases, the peak remains at about the same position down to 140 K, then starts to rapidly shift down in energy until reaching an energy of $E - E_F \approx -700$ meV at 100 K, temperature below which the peak does not evolve further. Upon heating, the QLS peak at the zone edges stays at $E - E_F \approx -700$ meV until about 120 K. Above this temperature the peak shifts rapidly up in energy until reaching its original high-temperature position at around 150 K.

On the other hand, the EDCs at Γ show an intense peak at $E - E_F \approx -400$ meV at 180 K. Its asymmetric line-shape, broader at energies above the peak towards E_F , corresponds to the superposition of the dispersive QP peak and the QLS. As temperature decreases and goes below 140 K, the spectral weight of this peak starts to rapidly decrease at energies above the peak, while the peak itself appears to shift down in energy until reaching $E - E_F \approx -800$ meV at 100 K, below which the peak does not change appreciably. From the momentum-resolved data, Fig. 3 of the main text, we know that the band minimum and effective mass of the QP state do not change with temperature. Only its intensity decreases upon entering the insulating state. Thus, the thermal evolution of the EDC at Γ actually corresponds to the superposition of two effects: the weight of the QP peak (fixed in energy) becomes weaker upon cooling into the insulating phase, while the peak of the QLS simultaneously shifts down in energy until reaching an energy lower than, but close to, the bottom of the original QP state. Upon heating, the behavior of the EDCs at Γ is reversed, however showing a hysteresis: only at temperatures above 120 K the peak starts to shift up in energy and gain spectral weight at energies higher than its position, until reaching its final energy position and lineshape at or above 150 K.

The energy of the MH/OV state at $E - E_F \approx -1.1$ eV remains temperature-independent within our resolution.

Fig. S9 presents the raw energy distribution curves (EDCs) along ΓZ ($k_{<111>}$) of the temperature-dependent data in another $V_2O_3(11\bar{2}0)$ thin film, different from the one discussed in the main text. One clearly sees how the dispersive QP peak at $T \gtrsim 160K$, Figs. S9(A, B), starts losing spectral weight upon cooling without changing its energy-

$V_2O_3 / Al_2O_3 (11\bar{2}0)$

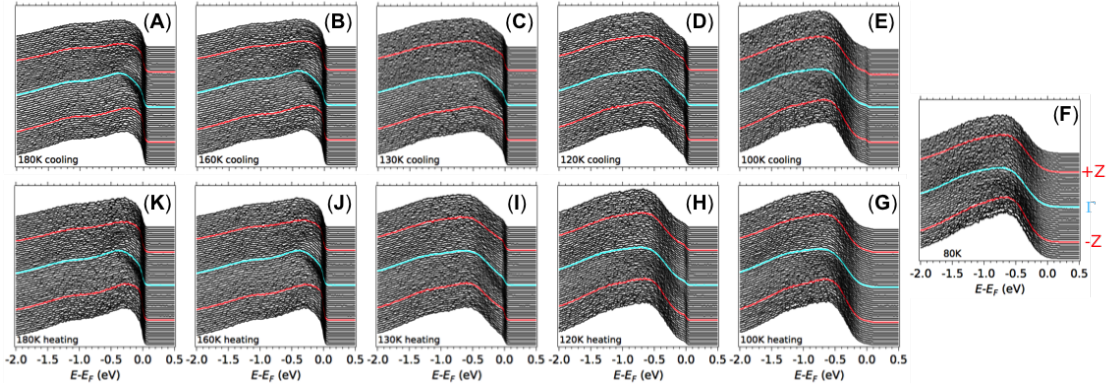


Figure S9. **Complementary temperature-dependent ARPES spectra.** (A-F) Raw EDC stacks along ΓZ ($k_{\langle 111 \rangle}$) when cooling from 180 K (metallic state) to 60 K (insulating state) in another $V_2O_3(11\bar{2}0)$ thin film, different from the one shown in the main text. (G-K) Corresponding spectra when heating back to 180K. The data were measured over an angular range allowing to probe states slightly beyond the Brillouin zone edges. EDCs at Γ and Z are shown in light blue and red, respectively. Measurements were performed at $h\nu = 86$ eV using linear horizontal polarization.

momentum dispersion –Figs. S9(C, D). Simultaneously, the broad QLS at $E - E_F \approx -250$ meV, best seen around the Z points, rapidly shifts down in energy when the temperature drops below about 160 K. At $T \lesssim 100K$, Figs. S9(E, F), the QP peak has essentially vanished, while the QLS has dropped to $E - E_F \approx -600$ meV. Upon heating, the dispersive QP peak re-emerges at a temperature between 120 K and 130 K, while the QLS band shifts up in energy. The thermal hysteresis in the spectral weight transfer between these two bands is best seen when comparing, for instance, panels (C) and (I) or panels (D) and (H).

Figures S10(A, B) focus on the EDCs from Fig. S9 at the Γ and $+Z$ points only. As the sample is cooled, panel (A), the peak of the QLS at $+Z$ shifts down in energy. When its energy becomes lower than the bottom of the dispersive QP band, this creates a downshift of the peak at Γ , which corresponds to the superposition of the QP band bottom and the QLS, and a concomitant decrease of its spectral weight at energies above the peak position. Upon heating, panel (B), the opposite behavior, with a clear hysteresis in the peak positions, is observed. All the data in this sample thus reproduce the essential observations described in the main text.

$\text{V}_2\text{O}_3/\text{Al}_2\text{O}_3(11\bar{2}0)$

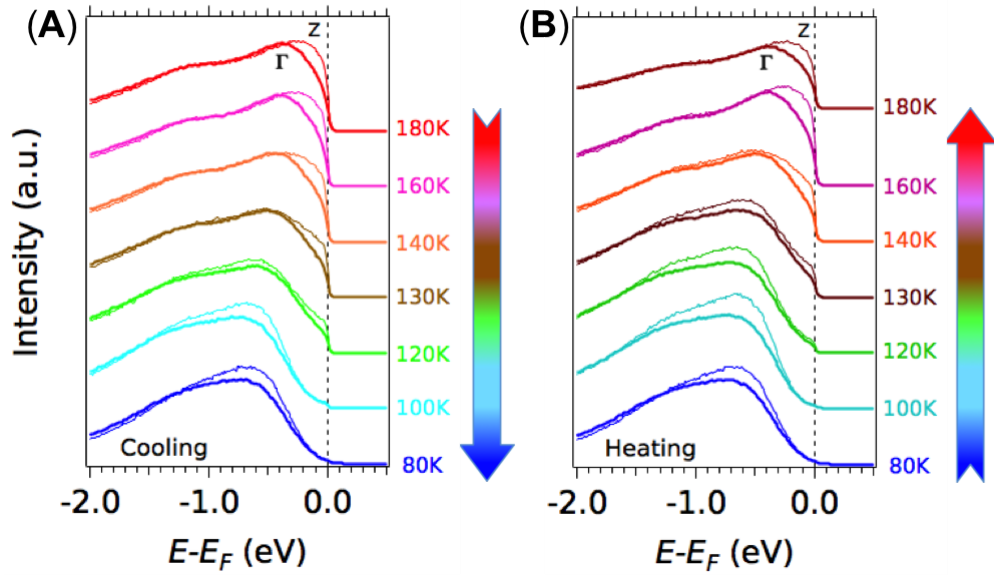


Figure S10. **Complementary temperature-dependent spectra at Γ and $+Z$.** (A, B) Energy distribution curves (EDCs) at Γ (thick lines) and $+Z$ (thin lines), integrated over 0.1 \AA^{-1} around each point, over a cooling and a heating cycle across the MIT, respectively. All data in this figure correspond to the spectra shown in Fig. S9 for a $\text{V}_2\text{O}_3(11\bar{2}0)$ thin film. Spectra at the same temperature on opposite thermal cycles are shown in slightly different color hues, for clarity.

Hysteresis in the momentum-integrated ARPES spectra

Fig. S11 shows the momentum-integrated ARPES spectra along ΓZ ($k_{\langle 111 \rangle}$) for $\text{V}_2\text{O}_3/\text{Al}_2\text{O}_3(01\bar{1}2)$ and $\text{V}_2\text{O}_3/\text{Al}_2\text{O}_3(11\bar{2}0)$ thin films, during cooling and heating cycles. As temperature lowers, the peak near E_F corresponding to the conduction band bundle, formed by the itinerant QP and the quasi-localized states, shifts down in energy until it reaches an energy $E - E_F \approx -800\text{meV}$, while the spectral weight of the Fermi step at E_F decreases until it ultimately disappears, thus creating the effect of a gap opening. The MH/OV band around $E - E_F = -1.1\text{eV}$ remains at a fixed energy. As the system is heated up again, the QP/LS peak shifts back towards E_F with a significant hysteresis in temperature, characteristic of first-order phase transitions. This is especially visible when comparing the EDCs between the heating and cooling processes, around 130K for the $\text{V}_2\text{O}_3/\text{Al}_2\text{O}_3(01\bar{1}2)$ sample, and around 145K for the $\text{V}_2\text{O}_3/\text{Al}_2\text{O}_3(11\bar{2}0)$ sample.

Finally, Fig. S12(A) shows the temperature-dependent fraction of insulating and metallic

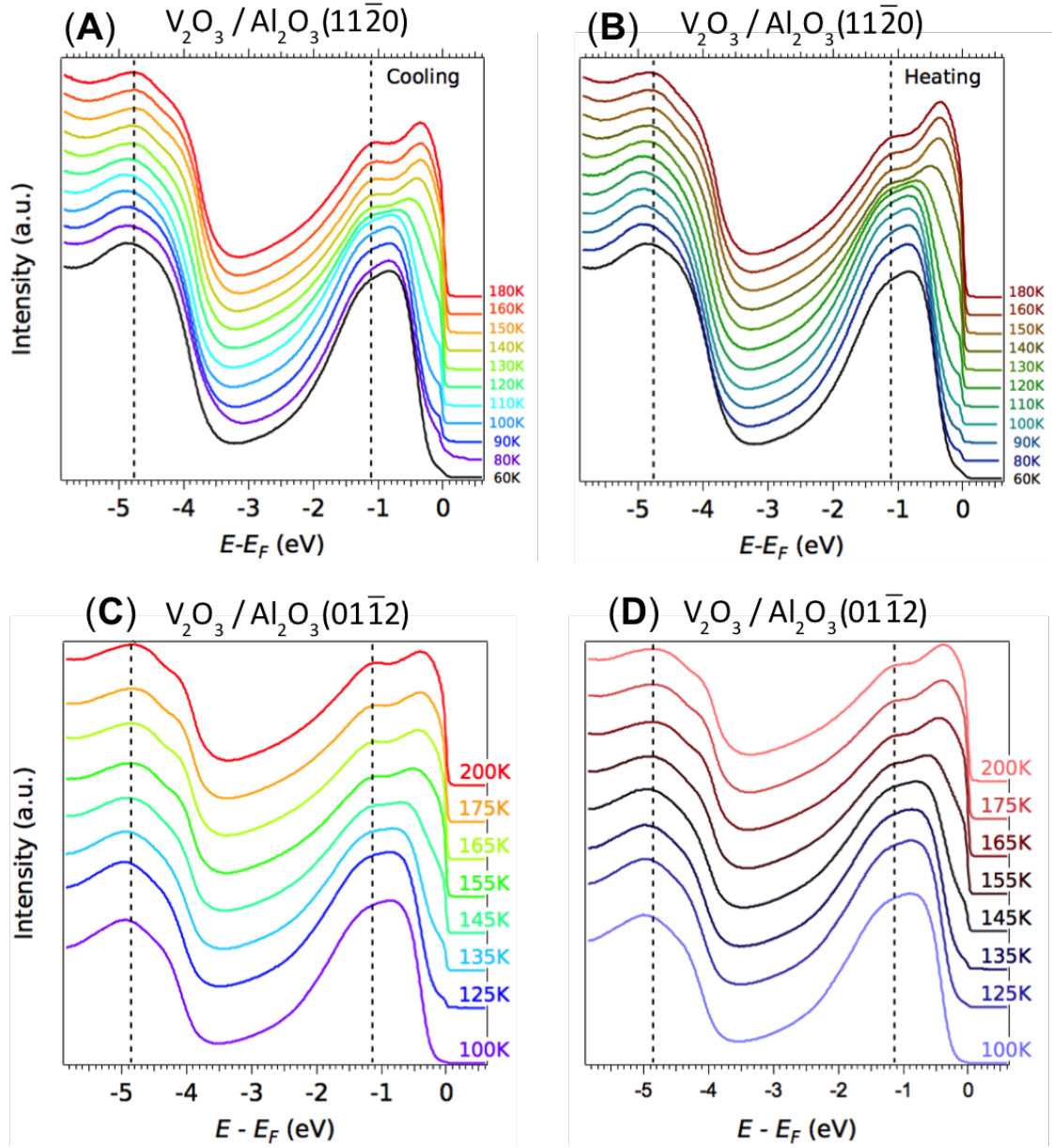


Figure S11. (Color online) **Hysteresis in the momentum-integrated ARPES spectra.** (A, B) Momentum-integrated EDCs on a $V_2O_3/Al_2O_3(11\bar{2}0)$ thin film, taken at different temperatures while cooling and heating through the MIT, respectively. (C, D) Analogous spectra measured on a $V_2O_3/Al_2O_3(01\bar{1}2)$ thin film. Dashed lines at $E - E_F \approx -4.8$ eV and $E - E_F \approx -1.1$ eV indicate the maxima of the valence band and MH/OV bands, respectively. Spectra at the same temperature on opposite thermal cycles are shown in slightly different color hues, for clarity.

domains extracted from the ARPES data of the $V_2O_3/Al_2O_3(01\bar{1}2)$ sample. Fig. S12(B) shows, for comparison, the resistance obtained on the same sample *after* ARPES measure-

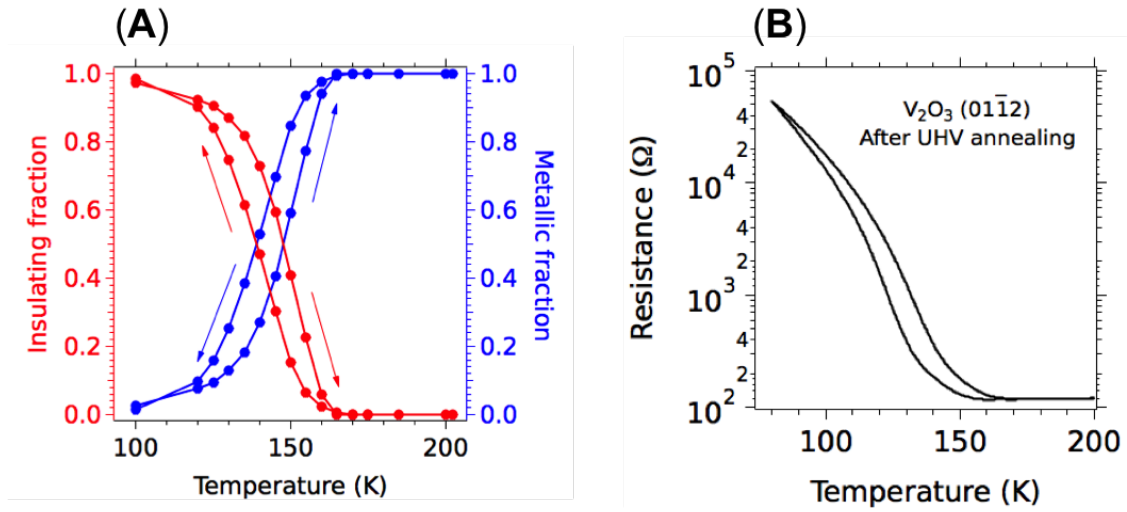
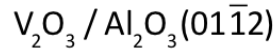


Figure S12. **Fraction of metallic and insulating spectral weights in the ARPES spectra of a V₂O₃/Al₂O₃(01 $\bar{1}$ 2) thin film.** (A) Representation of the fraction of insulating and metallic domains contributing to the ARPES intensity in the same V₂O₃/Al₂O₃(01 $\bar{1}$ 2) thin film of Figs. S11(C, D). Error bars in the fits, Eq. (1) of the main text, are smaller than the size of the symbols. (B) Resistance as a function of temperature measured in the same sample *after* UHV annealing and photoemission experiments.

ments.

* andres.santander-syro@universite-paris-saclay.fr

- [1] N. W. Ashcroft and N. Mermin, *Solid State Physics* (Brooks/Cole, 1976).
- [2] P. Fulde, *Correlated Electrons in Quantum Matter* (World Scientific, 2012)
<https://www.worldscientific.com/doi/pdf/10.1142/8419>.
- [3] N. F. Mott, Metal-insulator transition, *Rev. Mod. Phys.* **40**, 677 (1968).
- [4] D. B. McWhan, T. M. Rice, and J. P. Remeika, Mott transition in Cr-doped V_2O_3 , *Phys. Rev. Lett* **23**, 1384 (1969).
- [5] D. B. McWhan, J. P. Remeika, T. M. Rice, W. F. Brinkman, J. P. Maita, and A. Menth, Electronic specific heat of metallic Ti-doped V_2O_3 , *Phys. Rev. Lett.* **27**, 941 (1971).
- [6] N. F. Mott, *Metal-Insulator Transitions* (Taylor and Francis, London, 1990).
- [7] M. Imada, A. Fujimori, and Y. Tokura, Metal-insulator transitions, *Rev. Mod. Phys.* **70**, 1039 (1998).
- [8] V. Dobrosavljevic, N. Trivedi, and J. M. Valles, Jr., eds., *Conductor-Insulator Quantum Phase Transitions* (Oxford University, 2012).
- [9] M. J. Rozenberg, G. Kotliar, H. Kajueter, G. A. Thomas, D. H. Rapkine, J. M. Honig, and P. Metcalf, Optical conductivity in mott-hubbard systems, *Phys. Rev. Lett.* **75**, 105 (1995).
- [10] M. J. Rozenberg, G. Kotliar, and H. Kajueter, Transfer of spectral weight in spectroscopies of correlated electron systems, *Phys. Rev. B* **54**, 8452 (1996).
- [11] R. M. Moon, Antiferromagnetism in v_2o_3 , *Phys. Rev. Lett.* **25**, 527 (1970).
- [12] W. Bao, C. Broholm, G. Aeppli, P. Dai, J. M. Honig, and P. Metcalf, Dramatic switching of magnetic exchange in a classic transition metal oxide: Evidence for orbital ordering, *Phys. Rev. Lett.* **78**, 507 (1997).
- [13] V. I. Anisimov, D. E. Kondakov, A. V. Kozhevnikov, I. A. Nekrasov, Z. V. Pchelkina, J. W. Allen, S.-K. Mo, H.-D. Kim, P. Metcalf, S. Suga, A. Sekiyama, G. Keller, I. Leonov, X. Ren, and D. Vollhardt, Full orbital calculation scheme for materials with strongly correlated electrons, *Phys. Rev. B* **71**, 125119 (2005).
- [14] A. I. Poteryaev, J. M. Tomczak, S. Biermann, A. Georges, A. I. Lichtenstein, A. N. Rubtsov, T. Saha-Dasgupta, , and O. K. Andersen, Enhanced crystal-field splitting and orbital-selective coherence induced by strong correlations in V_2O_3 , *Phys. Rev. B* **76**, 085127 (2007).

- [15] J. Trastoy, A. Camjayi, J. del Valle, Y. Kalcheim, J.-P. Crocombette, D. A. Gilbert, J. A. Borchers, J. E. Villegas, D. Ravelosona, M. J. Rozenberg, and I. K. Schuller, Magnetic field frustration of the metal-insulator transition in V_2O_3 , *Phys. Rev. B* **101**, 245109 (2020).
- [16] Y. Kalcheim, A. Camjayi, J. del Valle, P. Salev, M. Rozenberg, and I. K. Schuller, Non-thermal resistive switching in Mott insulator nanowires, *Nat. Commun.* **11**, 2985 (2020).
- [17] S.-K. Mo, J. D. Denlinger, H.-D. Kim, J.-H. Park, J. W. Allen, A. Sekiyama, A. Yamasaki, K. Kadono, S. Suga, Y. Saitoh, T. Muro, P. Metcalf, G. Keller, K. Held, V. Eyert, V. I. Anisimov, and D. Vollhardt, Prominent quasiparticle peak in the photoemission spectrum of the metallic phase of V_2O_3 , *Phys. Rev. Lett.* **90**, 186403 (2003).
- [18] S.-K. Mo, H.-D. Kim, J. D. Denlinger, J. W. Allen, J.-H. Park, A. Sekiyama, A. Yamasaki, S. Suga, Y. Saitoh, T. Muro, and P. Metcalf, Photoemission study of $(V_{1-x}M_x)_2O_3$ ($M = Cr, Ti$), *Phys. Rev. B* **74**, 165101 (2006).
- [19] S. Shin, S. Suga, M. Taniguchi, M. Fujisawa, H. Kanzaki, A. Fujimori, H. Daimon, Y. Ueda, K. Kosuge, and S. Kachi, Vacuum-ultraviolet reflectance and photoemission study of the metal-insulator phase transitions in VO_2 , V_6O_{13} , and V_2O_3 , *Phys. Rev. B* **41**, 4993 (1990).
- [20] K. E. Smith and V. E. Henrich, Photoemission study of composition- and temperature-induced metal-insulator transitions in Cr-doped V_2O_3 , *Phys. Rev. B* **50**, 1382 (1994).
- [21] A. Georges and G. Kotliar, Hubbard model in infinite dimensions, *Phys. Rev. B* **45**, 6479 (1992).
- [22] I. Lo Vecchio, J. D. Denlinger, O. Krupin, B. J. Kim, P. A. Metcalf, S. Lupi, J. W. Allen, and A. Lanzara, Fermi surface of metallic V_2O_3 from angle-resolved photoemission: Mid-level filling of e_g^π bands, *Phys. Rev. Lett.* **117**, 166401 (2016).
- [23] I. Valmianski, J. G. Ramirez, C. Urban, X. Batlle, and I. K. Schuller, Deviation from bulk in the pressure-temperature phase diagram of V_2O_3 thin films, *Phys. Rev. B* **95**, 155132 (2017).
- [24] J. Trastoy, Y. Kalcheim, J. del Valle, I. Valmianski, and I. K. Schuller, Enhanced metal-insulator transition in V_2O_3 by thermal quenching after growth, *J. Mater. Sci.* **53**, 9131 (2018).
- [25] Y. Kalcheim, N. Butakov, N. M. Vargas, M.-H. Lee, J. del Valle, J. Trastoy, P. Salev, J. Schuller, and I. K. Schuller, Robust coupling between structural and electronic transitions in a Mott material, *Phys. Rev. Lett.* **122**, 057601 (2019).
- [26] T. C. Rödel, F. Fortuna, S. Sengupta, E. Frantzeskakis, P. L. Fèvre, F. c. Bertran, B. Mer-

- cey, S. Matzen, G. Agnus, T. Maroutian, P. Lecoeur, and A. F. Santander-Syro, Universal fabrication of 2D electron systems in functional oxides, *Advanced Materials* **28**, 1976 (2016).
- [27] S. Backes, T. C. Rödel, F. Fortuna, E. Frantzeskakis, P. Le Fèvre, F. Bertran, M. Kobayashi, R. Yukawa, T. Mitsuhashi, M. Kitamura, K. Horiba, H. Kumigashira, R. Saint-Martin, A. Fouchet, B. Berini, Y. Dumont, A. J. Kim, F. Lechermann, H. O. Jeschke, M. J. Rozenberg, R. Valentí, and A. F. Santander-Syro, Hubbard band versus oxygen vacancy states in the correlated electron metal SrVO₃, *Phys. Rev. B* **94**, 241110 (2016).
- [28] T. C. Rödel, M. Vivek, F. Fortuna, P. Le Fèvre, F. Bertran, R. Weht, J. Goniakowski, M. Gabay, and A. F. Santander-Syro, Two-dimensional electron systems in ATiO₃ perovskites (A=Ca, Ba, Sr): Control of orbital hybridization and energy order, *Phys. Rev. B* **96**, 041121 (2017).
- [29] P. Lömker, T. C. Rödel, T. Gerber, F. Fortuna, E. Frantzeskakis, P. Le Fèvre, F. Bertran, M. Müller, and A. F. Santander-Syro, Two-dimensional electron system at the magnetically tunable EuO/SrTiO₃ interface, *Phys. Rev. Materials* **1**, 062001 (2017).
- [30] T. C. Rödel, J. Dai, F. Fortuna, E. Frantzeskakis, P. Le Fèvre, F. Bertran, M. Kobayashi, R. Yukawa, T. Mitsuhashi, M. Kitamura, K. Horiba, H. Kumigashira, and A. F. Santander-Syro, High-density two-dimensional electron system induced by oxygen vacancies in ZnO, *Phys. Rev. Materials* **2**, 051601 (2018).
- [31] A. F. Santander-Syro, O. Copie, T. Kondo, F. Fortuna, S. Pailhès, R. Weht, X. G. Qiu, F. Bertran, A. Nicolaou, A. Taleb-Ibrahimi, P. L. Fèvre, G. Herranz, M. Bibes, N. Reyren, Y. Apertet, P. Lecoeur, A. Barthélémy, and M. J. Rozenberg, Two-dimensional electron gas with universal subbands at the surface of SrTiO₃, *Nature* **469**, 189 (2011).
- [32] A. F. Santander-Syro, C. Bareille, F. Fortuna, O. Copie, M. Gabay, F. Bertran, A. Taleb-Ibrahimi, P. L. Fèvre, G. Herranz, N. Reyren, M. Bibes, A. Barthélémy, P. Lecoeur, J. Guevara, and M. J. Rozenberg., Orbital symmetry reconstruction and strong mass renormalization in the two-dimensional electron gas at the surface of KTaO₃, *Phys. Rev. B* **86**, 121107 (2012).
- [33] M. Takizawa, M. Minohara, H. Kumigashira, D. Toyota, M. Oshima, H. Wadati, T. Yoshida, A. Fujimori, M. Lippmaa, M. Kawasaki, H. Koinuma, G. Sordi, and M. Rozenberg, Coherent and incoherent *d* band dispersions in SrVO₃, *Phys. Rev. B* **80**, 235104 (2009).
- [34] M. Qazilbash, M. Brehm, B.-G. Chae, P.-C. Ho, G. Andreev, B.-J. Kim, S. Yun, A. Balatsky, M. Maple, F. Keilmann, H.-T. Kim, and D. Basov, Mott transition in VO₂ revealed by infrared

- spectroscopy and nano-imaging, *Science* (New York, N.Y.) **318**, 1750 (2008).
- [35] A. McLeod, E. Heumen, J. Ramirez, S. Wang, T. Saerbeck, S. Guenon, M. Goldflam, L. Andereg, P. Kelly, A. Mueller, M. Liu, I. Schuller, and D. Basov, Nanotextured phase coexistence in the correlated insulator V_2O_3 , *Nature Physics* **13**, 80 (2016).
- [36] S. Lupi, L. Baldassarre, B. Mansart, A. Perucchi, A. Barinov, P. Dudin, E. Papalazarou, F. Rodolakis, J. P. Rueff, J. P. Itié, S. Ravy, D. Nicoletti, P. Postorino, P. Hansmann, N. Paragh, A. Toschi, T. Saha-Dasgupta, O. K. Andersen, G. Sangiovanni, K. Held, and M. Marsi, A microscopic view on the Mott transition in chromium-doped V_2O_3 , *Nat. Commun.* **1**, 105 (2010).
- [37] B. A. Frandsen, L. Liu, S. C. Cheung, Z. Guguchia, R. Khasanov, E. Morenzoni, T. J. S. Munsie, A. M. Hallas, M. N. Wilson, Y. Cai, G. M. Luke, B. Chen, W. Li, C. Jin, C. Ding, S. Guo, F. Ning, T. U. Ito, W. Higemoto, S. J. L. Billinge, S. Sakamoto, A. Fujimori, T. Murakami, H. Kageyama, J. A. Alonso, G. Kotliar, M. Imada, and Y. J. Uemura, Volume-wise destruction of the antiferromagnetic Mott insulating state through quantum tuning, *Nature Communications* **7**, 12519 (2016).
- [38] M. M. Qazilbash, A. A. Schafgans, K. S. Burch, S. J. Yun, B. G. Chae, B. J. Kim, H. T. Kim, and D. N. Basov, Electrodynamics of the vanadium oxides VO_2 and v_2O_3 , *Phys. Rev. B* **77**, 115121 (2008).
- [39] M. K. Stewart, D. Brownstead, S. Wang, K. G. West, J. G. Ramirez, M. M. Qazilbash, N. B. Perkins, I. K. Schuller, and D. N. Basov, Insulator-to-metal transition and correlated metallic state of V_2O_3 investigated by optical spectroscopy, *Phys. Rev. B* **85**, 205113 (2012).
- [40] I. Lo Vecchio, L. Baldassarre, F. D'Apuzzo, O. Limaj, D. Nicoletti, A. Perucchi, L. Fan, P. Metcalf, M. Marsi, and S. Lupi, Optical properties of v_2O_3 in its whole phase diagram, *Phys. Rev. B* **91**, 155133 (2015).
- [41] J.-H. Park, L. H. Tjeng, A. Tanaka, J. W. Allen, C. T. Chen, P. Metcalf, J. M. Honig, F. M. F. de Groot, and G. A. Sawatzky, Spin and orbital occupation and phase transitions in V_2O_3 , *Phys. Rev. B* **61**, 11506 (2000).
- [42] F. Rodolakis, P. Hansmann, J.-P. Rueff, A. Toschi, M. W. Haverkort, G. Sangiovanni, A. Tanaka, T. Saha-Dasgupta, O. K. Andersen, K. Held, M. Sikora, I. Alliot, J.-P. Itié, F. Baudelet, P. Wzietek, P. Metcalf, and M. Marsi, Inequivalent routes across the Mott transition in V_2O_3 explored by x-ray absorption, *Phys. Rev. Lett.* **104**, 047401 (2010).

- [43] D. Grieger and M. Fabrizio, Low-temperature magnetic ordering and structural distortions in vanadium sesquioxide V_2O_3 , *Phys. Rev. B* **92**, 075121 (2015).
- [44] F. Lechermann, N. Bernstein, I. I. Mazin, and R. Valentí, Uncovering the mechanism of the impurity-selective Mott transition in paramagnetic V_2O_3 , *Phys. Rev. Lett.* **121**, 106401 (2018).
- [45] A. I. Poteryaev, M. Ferrero, A. Georges, and O. Parcollet, Effect of crystal-field splitting and interband hybridization on the metal-insulator transitions of strongly correlated systems, *Phys. Rev. B* **78**, 045115 (2008).
- [46] P. Zhang, P. Richard, T. Qian, Y.-M. Xu, X. Dai, and H. Ding, A precise method for visualizing dispersive features in image plots, *Rev. Sci. Instr.* **82**, 043712 (2011).